WSR: A WiFi Sensor for Collaborative Robotics

Ninad Jadhav[1*], Weiying Wang[1*], Diana Zhang[2], Oussama Khatib[3], Swarun Kumar[2] and Stephanie Gil[1]

Abstract

In this paper we derive a new capability for robots to measure relative direction, or Angle-of-Arrival (AOA), to other robots, while operating in non-line-of-sight and unmapped environments, without requiring external infrastructure. We do so by capturing all of the paths that a WiFi signal traverses as it travels from a transmitting to a receiving robot in the team, which we term as an *AOA profile*. The key intuition behind our approach is to *emulate antenna arrays in the air* as a robot moves freely in 2D or 3D space. The small differences in the phase and amplitude of WiFi signals are thus processed with knowledge of a robots' local displacements (often provided via inertial sensors) to obtain the profile, via a method akin to Synthetic Aperture Radar (SAR). The main contribution of this work is the development of i) a framework to accommodate arbitrary 2D and 3D trajectories, as well as continuous mobility of both transmitting and receiving robots, while computing AOA profiles between them and ii) an accompanying analysis that provides a lower bound on variance of AOA estimation as a function of robot trajectory geometry that is based on the Cramer Rao Bound and antenna array theory. This is a critical distinction with previous work on SAR that restricts robot mobility to prescribed motion patterns, does not generalize to the full 3D space, and/or requires transmitting robots to be static during data acquisition periods. In fact, we find that allowing robots to use their full mobility in 3D space while performing SAR, results in *more accurate* AOA profiles and thus better AOA estimation. We formally characterize this observation as the *informativeness of the trajectory*; a computable quantity for which we derive a closed form. All theoretical developments are substantiated by extensive simulation and hardware experiments on air/ground robot platforms. Our experimental results bolster our theoretical findings, demonstrating that 3D trajectories provide enhanced and consistent accuracy, with AOA error of less than $10 \deg$ for 95% of trials. We also show that our formulation can be used with an off-the-shelf trajectory estimation sensor (Intel RealSense T265 tracking camera), for estimating the robots' local displacements, and we provide theoretical as well as empirical results that show the impact of typical trajectory estimation errors on the measured AOA. Finally, we demonstrate the performance of our system on a multi-robot task where a heterogeneous air/ground pair of robots continuously measure AOA profiles over a WiFi link to achieve dynamic rendezvous in an unmapped, 300 square meter environment with occlusions.

Keywords
Multi-robot systems, WiFi, wireless sensing, Robotics, Sensor

1 Introduction

Multi-robot coordination often requires robots to gather information about neighboring robots and their shared environment in order to collaborate effectively. Sensing relative state between robots, such as their relative positions, proximity, or nature (friend or foe) is often needed for coordination. This information is critical for various multi-robot applications, ranging from coverage, to exploration, to rendezvous and beyond (Cortes et al., 2004; Almadhoun et al., 2019; Cunningham et al., 2012; Freda et al., 2019; Choudhary et al., 2017a; Grisetti et al., 2010). However, how to obtain this information in an unknown and unmapped environment, without line-of-sight and without GPS or other external infrastructure, is an open challenge. A promising approach for obtaining relative position related information locally, exploits information extracted from exchanged wireless signals (Gil et al., 2015a). As a wireless signal travels between robots, it physically interacts with the environment. Its amplitude and phase is affected by the

distance it travels, the obstacles it passes through or is reflected off of, and the relative positions and velocities of the communicating robots in a phenomenon called *multipath*. This multipath can be measured as an Angle-of-Arrival (AOA) profile, where the arriving signal's *direction and power along each path* is measured as peaks along different spatial angles (see Fig. 1), for a pair of communicating robots in a team. Measuring these AOA profiles would thus allow robots to obtain information about the relative direction of other robots that they are able to receive any

---

[1]Harvard University, US
[2]Carnegie Mellon University, US
[3]Stanford University, US
[*]are co-primary authors

Corresponding author:
Ninad Jadhav, REACT Lab, Harvard University, Boston, MA, US.
Weiying Wang, REACT Lab, Harvard University, Boston, MA, US
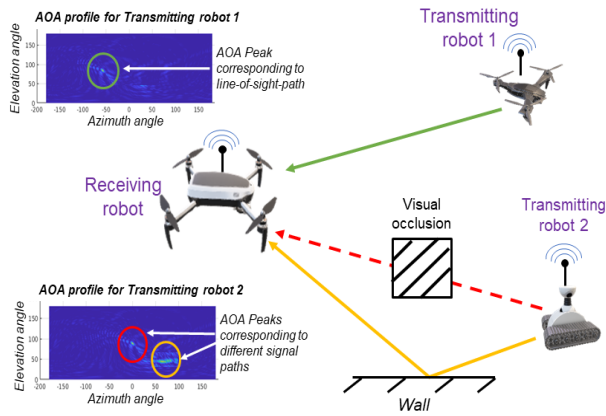Email: {njadhav, weiyingwang}@g.harvard.edu

Figure 1. *Schematic representation of AOA profiles obtained by a signal receiving UAV for transmitting aerial and ground robot. Green, Red and orange lines represent the line-of-sight, direct and reflected signal paths respectively. These multipaths are captured in the corresponding AOA profiles as different AOA peaks.*

communication from, including lightweight ping packets. *We note that ping packets incur a very small fraction of available bandwidth, as little as 5 KB/s; thus robots can perform AOA estimation of one another at much longer distances, and through occlusions, even if they are not able to communicate other information, such as maps, typically requiring much higher bandwidths (Schmuck and Chli, 2019).* In this way, wireless signals could inform about a distant or occluded neighboring robot which would be difficult or impossible to obtain using traditional on-board sensors alone such as LiDAR or camera.

Previous work has shown that measuring AOA profiles is possible, and that incorporating this information into multi-robot systems can be used address several important long-standing challenges in robotics. For example: i) several AOA profiles collected from the same transmitting source can be used to triangulate the position of the sender, leading to accurate positioning and tracking in GPS-denied environments (Kumar et al., 2014a; Kotaru et al., 2015; Xiong and Jamieson, 2013a; Adib et al., 2014; Vasisht et al., 2016; Adib and Katabi, 2013; Karanam and Mostofi, 2017), ii) an AOA profile can be used by robots to find several directions of motion that would improve communication quality to another agent in the team, allowing for more reliable communication in complex and cluttered environments (Gil et al., 2015a; Wang et al., 2019), and iii) capturing the full multipath *signature* of the sender via its AOA profile can be used to verify the uniqueness of a sender with implications for security and authentication in multi-agent systems (Gil et al., 2015b; Xiong and Jamieson, 2013b). However, a main limitation of many of these approaches is that they do not extend to general robotics platforms and full 3D mobility of multiple agents, while maintaining the ability to collect AOA profile information. *In order to achieve true adoption of this novel mode of sensing over communication signals in robotics, we need to resolve these important limitations which is the goal of the current paper.* In this paper we do not focus on a particular application domain but rather focus on the development of their critical primitive – AOA profile measurement capabilities and the characterization of their

attainable accuracy – for general air/ground multi-robot systems.

We develop an algorithmic and theoretical framework for measuring full AOA profiles between robots that are i) communicating locally over a peer-to-peer standard WiFi network, ii) using only on-board sensors native to robotic platforms, namely, WiFi and a trajectory estimation sensor, and iii) freely mobile in 3D space. This framework would constitute a highly amenable design for fully distributed robotic systems. The key intuition for our approach builds off of Synthetic Aperture Radar (SAR) to measure small phase and amplitude differences of a transmitted WiFi signal as the receiving robot moves through space. In this way, the robot effectively emulates *"antenna arrays in the air,"* (See Fig. 2) tracing out a virtual multi-antenna array (with one "antenna element" for each received packet) whose shape or *array geometry* is dictated by the *path traversed* by the robot. Antenna array theory indicates that a full AOA profile can be reconstructed from an array of short length of the order of signal wavelength (about 6cm for 5GHz WiFi) (Orfanidis, 2016). This allows the receiving robot to resolve the incoming signal directions, using small displacements (sub-trajectories), as it moves through space. **This paper shows for the first time that arbitrary trajectories on general air/ground robotic platforms are indeed compatible with SAR-type approaches**.

Advances in accurate pose estimation of local robot trajectories using on-board sensors such as camera and LiDAR (Schmuck and Chli, 2019; Choudhary et al., 2017b; Qin et al., 2018) enable this new possibility of applying SAR over *arbitrary* 2D and 3D trajectories on robot platforms. However, key challenges must be addressed. Namely, whether SAR-type approaches can be successfully employed over i) arbitrary 3D trajectories subject to trajectory estimation error, and ii) in a scenario where both the transmitting and receiving robot are moving simultaneously, was not known.

1.1 Key challenges and approach

We simultaneously address the challenges and opportunities imposed by arbitrary robot motion by appealing to antenna array theory (Vu et al., 2011). We first formulate a SAR equation to effectively isolate the phase change in the signal resulting from any arbitrary 2D or 3D robot trajectory. Isolation here refers to isolation of the phase change from other sources of noise, such as carrier frequency offset (CFO), and/or simultaneous mobility at the transmitting and receiving robots i.e *moving ends*. Thus our developed methods allow for continuous data collection and AOA profile estimation, between any robots that can communicate (even at low rates of 5kB/s).

Interestingly, the ability to perform SAR over arbitrary 3D robot trajectories holds potential for *improving the accuracy of AOA profiles*. Thus, one key question that we address in this work is: *how to relate the informativeness of a robot's trajectory to the resulting AOA profile?* It is well known that different antenna array geometries display different sensitivity to measuring phase differences in a received signal (Manikas, 2004). Hence, it is intuitive to expect that *different robot trajectories should also impact the AOA profile and specifically the accuracy of the AOA peak that*
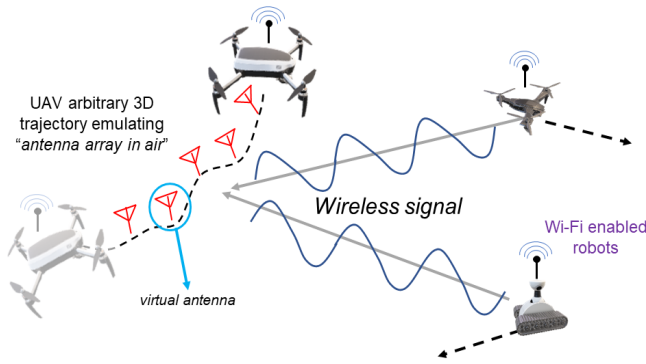
UAV arbitrary 3D
trajectory emulating
"*antenna array in air*"

virtual antenna

Wireless signal

Wi-Fi enabled
robots

Figure 2. *A schematic representation of our approach that enables robots to sense relative direction of other robots using local trajectory and wireless signal information to emulate a virtual antenna array. The dotted black lines indicate arbitrary robot trajectory paths in 2D and 3D.*

corresponds to the direction of maximum power path of received signal. We formalize this intuition via a Cramer Rao Bound analysis. The Cramer Rao Bound (CRB) captures the sensitivity of AOA peak estimation, as it is a lower bound on its variance, resulting from a particular array geometry. In particular, the CRB is proportional to the inverse of the *Fisher Information* for a specific antenna array geometry. We thus treat the inverse of the CRB as the *informativeness* of the antenna array and seek to characterize this value for different trajectories. Along these lines we derive a new form of the CRB for analyzing the effect of arbitrary trajectory geometry on the quality of the resulting AOA estimation. Our analysis reveals that indeed the ability to compute AOA profiles over a robot's arbitrary 3D trajectories provides a precise advantage as 3D trajectories are highly informative when compared to 2D trajectories.

Additionally, we derive the necessary theory to analyze the impact of the robot's trajectory estimation error, resulting from the use of on-board sensors, on the AOA estimation accuracy. Our theoretical development shows that trajectory drift and high frequency noise about the estimated trajectory mean manifests itself as a shift and attenuation of maximum magnitude AOA peak in the resulting profile, which we characterize. Moreover, we show that using short sub-trajectories makes our system resilient to long-term drift accumulation in the entire estimated robot trajectory.

Our analysis reveals several surprising insights about the nature of how such robot trajectories influence AOA profiles, some of which are described below:

- **AOA profile reconstruction using arbitrary robot motion:**. A single short local trajectory can be used to simultaneously measure AOA profiles for *all* communication neighbor robots j for a given robot i.
- **Informativeness of robot trajectories:** A random curved trajectory in 3-D space of a given length is more informative (as determined by the CRB) than a regular linear trajectory, as might typically be prescribed for SAR. Hardware experiments support this analysis showing less than 10 deg error in AOA for 95% of trials for arbitrary 3D trajectories, whereas for planar 2D curved and linear trajectories only 50%

and 7% of trials show error below 10 deg respectively (c.f. Section 7.1).

- **Influence of trajectory estimation error on AOA estimation accuracy:** AOA estimation will suffer a shift Δ and a peak attenuation of $\cos(\sigma/2)$ where Δ is linearly proportional to the trajectory drift and σ is the maximum angular variation of the trajectory estimation error about its mean (c.f. Lemma 3). Our hardware experiments indicate that this translates to an estimation error of 10.03 degree in azimuth, 2.23 degree in elevation (use Fig. 3 schematic for reference) on average for 6% absolute trajectory error (0.06m trajectory estimation error for a 1.2m robot displacement) using an Intel RealSense T265 off-the-shelf tracking camera.
- **AOA profile estimation with moving ends:** Obtaining AOA estimation using a SAR-based technique is possible even when both the transmitting and receiving robots are mobile during the signal sampling phase. We show that this is due to the translation agnostic property of phase change in wireless signals. AOA estimation can thus be accomplished under certain conditions (that we define) so long as robots can share their position estimates in their own local reference frame (c.f. Lemma 1).

We substantiate the above observations with quantitative theoretical bounds on errors. These are further validated with extensive hardware experiments, demonstrating agreement in theory and in practice for every derived claim in the paper. Our implementation uses an off-the-shelf 5Ghz WiFi card, tracking camera, and a local-peer-to-peer network with no pre-installed wireless routers – thereby demonstrating how our methods are designed for distributed implementation and seamless integration on today's robot platforms.

1.2 Paper contributions

In this paper we:

1. Develop the algorithmic machinery for using estimated local robot 3D trajectories for achieving incoming signal direction, or AOA profile estimation (Fig. 3).
2. Derive the algorithmic framework for allowing simultaneous motion of both ends (transmitting and receiving robots) while obtaining a full and accurate AOA profile. This accommodates continuous motion and continuous AOA estimation during robot operation.
3. Develop the theory to characterize the impact of i) the robots' trajectory on the informativeness and accuracy of the AOA estimation and ii) trajectory estimation error on the AOA estimation error.
4. Support all theory and algorithmic claims with in-depth hardware experiments, including a proof-of-concept application where robots use locally measured AOA to achieve fully dynamic rendezvous between an aerial drone and an occluded ground robot.

1.3 Paper roadmap

In the next section we provide a summary of previous work done in the context of robotics and wireless signal. Sec. 4
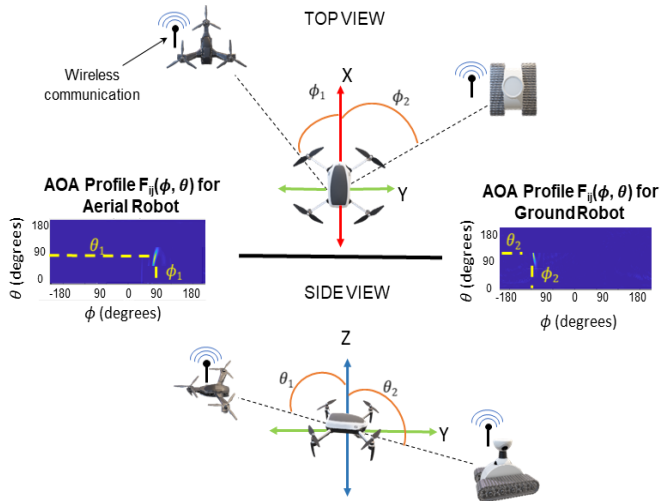
Figure 3. *Schematic showing AOA profile obtained by signal receiving UAV for transmitting ground and aerial robots. The Angle-of-Arrival (ϕ, θ) in azimuth (top view) and elevation (side view) respectively obtained from these profiles is highlighted in yellow.*

Figure 4. *Aerial and ground robots used in hardware experiments equipped with different off-the-shelf on-board sensors. Each robot is equipped with an UP Squared on-board compute device that has Intel 5300 WiFi card, an omnidirectional antenna, and an Intel RealSense T265 tracking cameras.*

formally states the problem statements and the definitions relevant to our development and analysis. Sec. 4 details the formulation of arbitrary 3D SAR and Sec. 6 shows how our system can handle signal transmitter robots that are mobile. Sec. 7 provides an analysis of the different factors that impact AOA calculation. We show the results of our hardware experiments in Sec. 8 and evaluate the capability of our system using a proof-of-concept application in Sec. 9. Finally, we provide directions for future research and concluding remarks in Sec. 10 and 11 respectively.

2 Related Work

In this section, we provide an overview of prior work on applications of wireless signals, specifically in the context of robotics. We first highlight some of the limitations of traditional sensors in obtaining relative information in multi-robot systems, as well as developments in wireless community that explore the use of wireless signals as a sensing modality. Next we look at previous approaches on obtaining relative direction information between communicating robots, the corresponding open challenges and the underlying enabling research from antenna array theory and computer vision.

Relative state estimation in multi-robot systems: Many multi-robot coordination problems such as coverage (Cortes et al., 2004), mapping (Tapus and Siegwart, 2005; Schmuck and Chli, 2017; Se et al., 2001; Fenwick et al., 2002), frontier exploration (Gautam et al., 2017; Solanas and García, 2004; Fox et al., 2006; Burgard et al., 2000), and persistent surveillance (Nigam et al., 2012; Stump and Michael, 2011) rely on knowledge of relative positions and other state information between collaborating robots. This information can be obtained from on-board GPS devices or other sensors such as camera and LiDAR that provide information of other agents' relative poses as well as about the environment; a capability useful for many of the stated collaboration tasks, but they have important
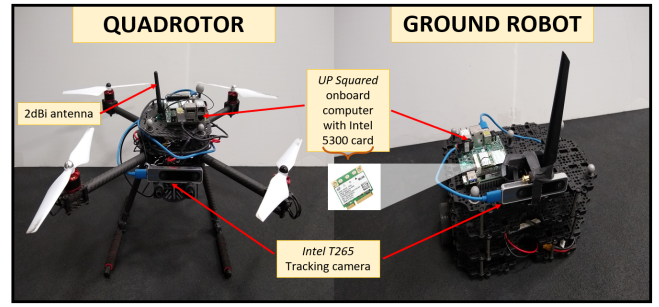
limitations. In particular they often don't work in GPS-denied and communication constrained environments, non-line-of-sight, over long distances, and/or when there is a lack of a shared coordinate frame and map. Thus, for many common environments such as those with clutter, those that require robots to operate at far distances from one another or the ones that lack common features required for fixing a shared coordinate frame, the current sensing methods easily get disoriented (SajadSaeedi et al., 2016; Kshirsagar et al., 2018).

Sensing using wireless signals: Going beyond traditional sensors, a robotic platform can we equipped with different types of wireless communication hardware (Calvo-Fullana et al., 2019). Beyond enabling communication, wireless signals processing has shown great promise for sensing as well. For example, it has been shown that transmitted wireless signals between devices can be used to extract useful information such as device position (Kotaru et al., 2015; Xiong and Jamieson, 2013a; Kumar et al., 2014b; Wang and Katabi, 2013; Karanam et al., 2018; Cominelli et al., 2019; Verma et al., 2018). Beyond localization, recent work has shown the ability to sense rich information about the environment as well, from tracking and imaging behind walls (Adib et al., 2015; S. Depatla and Mostofi, 2017; Adib and Katabi, 2013; Gonzalez-Ruiz and Mostofi, 2013), to materials sensing (Zhang et al., 2019; Ha et al., 2020; Dhekne et al., 2018), imaging in harsh visual conditions (Guan et al., 2020) and even shape sensing (Jin et al., 2018). While these works undoubtedly show the promise of using wireless signals to obtain useful information about a robots' state and its environment in ways that more traditional sensors like cameras and LiDAR cannot, they are not necessarily compatible with general robotics applications. These methods sometimes use specialized hardware, specialized wireless signals and non 802.11 protocols (that may not be WiFi which are most readily available on robot platforms) or pre-deployed infrastructure. Often, they also do not consider mobility (both signal transmitting and receiving robot), which can have a profound impact on the accuracy of these methods. As such, they are not inherently designed to be seamlessly integrated with robotic platforms.

Some WiFi based methods use Received Signal Strength (RSS), which refers to the magnitude of the signal (Zhu and Feng, 2013). However capturing substantial changes

in signal magnitude require large displacements of the receiving robot and/or requires sampling along multiple directions. This makes RSS coarse and hence ill-suited for extracting information with accuracy and precision over short robot displacements. Another possibility is to use *Channel State Information* (CSI) - information obtained from the PHY layer of 802.11 protocol (Halperin et al., 2010). CSI essentially facilitates capturing the phase of a wireless signal which is very sensitive to even small amount of displacements. It thus provides more granularity of information as compared to RSS (Yang et al., 2013; Ma et al., 2019).

Synthetic Aperture Radar (SAR): Using mobility of robots can improve the quality of information obtained (Twigg et al., 2019). SAR is also an alternative solution to obtain information from wireless signals that leverages mobility of signal receivers (Fitch, 1988). Applications for imaging that use RADAR-based SAR, generally use controlled linear motion of robot arm or alternatively they mount a vertical linear array on the robot (Watts et al., 2016; Barrie, 2004). On the other hand, our previous work *exploits mobility* and WiFi signals, both inherent to robotic platforms, to emulate a virtual antenna array along the trajectory of the robot, a method akin to SAR for accurately measuring the change in phase of an incoming signal. As WiFi signals traverse between a transmitting robot and a receiving robot, they interact with the environment such as being absorbed, reflected, and scattered (Goldsmith, 2005) by objects in the environment. Therefore, the signal paths a particular communicated message takes through the environment if properly resolved, can reveal information about the direction of the transmitting robot. This proves useful in absence of a global reference frame where the robots are separated by large distances and/or are occluded by objects in the environment. Indeed, exploiting this fact has led to many uses like positioning (Kumar et al., 2014a), adaptive networking (Gil et al., 2015a), mapping (Wang et al., 2019), and security (Gil et al., 2015b; Wheeler et al., 2019; Gil et al., 2019). These works use position information from simple linear motion or 2D circular trajectories (e.g. turn-in-place) obtained using IMU and require that the transmitting robot should be static over the data collection period of a few seconds.

However, emulating a linear or circular antenna array leads to *sensing ambiguities* where the receiver robot in unable to distinguish between two (or more) transmitter robot directions. For example, a linear antenna array will exhibit left/right ambiguity and a planar 2D antenna cannot not differentiate between a source in the plane above the array versus a source in the plane below the array. This is a well know problem in antenna array theory (Manikas, 2004, chapter 6). Antenna array research shows a possible solution of using 3D antenna arrays that are capable of resolving such ambiguities (Vu et al., 2011, 2010), but this requires emulating an arbitrary shaped 3D array using position information from on-board sensors. Another open challenge not addressed by previous works is the possible mobility of the transmitting robot for the duration of SAR. The change in phase measurements for even small displacements (e.g 24cm) of the receiving robot is desirable for obtaining highly

accurate AOA profile (Gil et al., 2015a). However if the simultaneous motion of the transmitting robot on the same scale, if not accounted for, leads to phase shift of $2*\pi$ resulting in considerable errors in phase measurements for the receiving robot. These factors are important motivators for developing the ability for robots to *emulate 3D antenna arrays over their arbitrary paths as they traverse the environment while both ends (i.e transmitting and receiving robots) remain mobile at all times.*

Trajectory estimation: Advances in vision-based sensing and optimization in the past couple of years allow for obtaining accurate local trajectory estimates. Monocular systems such as (Qin et al., 2018), utilize one camera and one low-cost inertial measurement unit as sensing components, achieving 0.21m ATE in a 500m real world trajectory. Pose Graph Optimization also plays an essential role in state-of-the-art SLAM tasks as a back-end optimizer, for example as with distributed mapping (Choudhary et al., 2017b) and rotation estimation (Carlone et al., 2015). Energy-efficient accelerator for VIO in (Suleiman et al., 2018, 2019) also enables the localization and mapping on miniaturized robots. Several other works (Ma and Karaman, 2018; Gallego et al., 2018; Sabzevari and Scaramuzza, 2016) provide a multitude of techniques ranging from specialized visual sensing capability to estimation of depth and motion in the view with monocular system.

Antenna array theory: Traditional antenna arrays that provide AOA information are often bulky and hence not suitable for small agile robot platforms (Björnson et al., 2019). To this end, we consider a SAR inspired approach that uses robot motion and signal measurements over several communicated packets, to obtain a full AOA profile. This paper builds closely off of antenna array theory in order to characterize AOA performance metrics resulting from 3D SAR applied arbitrary robot trajectory in 3D space. The Cramer Rao Bound (CRB) is a often utilized tool for the performance analysis of different antenna array geometries(Gazzah and Marcos, 2006; Mirkin and Sibul, 1991). Specifically, the CRB provides important lower bounds estimates on the variance of the resulting angle-of-arrival estimates as a function of antenna array geometry (Moriya et al., 2012; Mohamed et al., 2019); in other words, CRB analysis *reveals the relationship between the robot trajectory and the richness of information attainable from processing received communication signals.* This key observation opens the possibility of thinking of SAR as an enabling technology for a new kind of *sensing* for robotics.

Thus, in comparison to previous work done in SAR, our proposed system is a generalized formulation of a direction finding capability for robots that combines local trajectory estimation methods with antenna array theory. It enables a robot to obtain relative AOA of a WiFi signal transmitter (stationary or moving) by using arbitrary 3D motion. However, this requires a mathematical, algorithmic, and experimental framework for characterizing the impact of i) 3D trajectories on the informativeness (or richness of information) derived from processing collected WiFi signals, ii) error in trajectory estimation on the resulting accuracy of

the AOA estimates, and iii) mobility at *both ends* meaning mobility of both the transmitting and receiving robots, in order to enable continuous data collection that is most compatible with general multi-robot tasks. We address these objectives in the current paper.

3 Background and Notation

In this section we present important notational conventions used as well as essential background on wireless signals and Synthetic Aperture Radar (SAR) that we will use throughout.

3.1 Coordinate system

As our system returns angular information, we formulate our problem in a spherical coordinate system. Fig. 5 shows a schematic representation of a robot trajectory and it's local spherical coordinate system. φ and ξ are the azimuth and elevation angles of the receiving robot i at a given position along it's trajectory. The AOA tuple (ϕ, θ) represents the transmitting robot's relative azimuth and elevation direction with respect to the initial position (at time t_k) of robot i. ϕ and φ are measured counter-clockwise from the x-axis while θ and ξ are measured clockwise from z-axis. Robot i's position at time t denoted by $p_i(t)$, is represented as $(\rho_i(t), \varphi_i(t), \xi_i(t))$. In the case that the robot trajectory is obtained via on-board sensors or estimation techniques the positions are denoted by $\hat{p}_i(t)$. This position measurement is subject to error which we denote as κ_ρ, κ_ϕ and κ_θ for errors in ρ, φ, ξ respectively. We denote estimated relative AOA (from our system) between robots i and j as $(\hat{\phi}, \hat{\theta})$ and the true AOA (from motion capture system) as (ϕ_g, θ_g). Our experimental evaluation uses Cartesian coordinates for robot's position, represented as $(x_i(t), y_i(t), z_i(t))$.*

3.2 Robot trajectory

For our experiments, robot positions are generally collected via trajectory estimation techniques using on-board sensors or from external motion capture system (groundtruth). We define a groundtruth local *sub-trajectory* $\chi_i(t)$ of the robot i over which we intend to perform AOA estimation, as the trajectory of positions corresponding to $t \in [t_k, \ldots, t_l]$ as shown in Fig. 5. An estimated trajectory is denoted as $\hat{\chi}_i(t)$. We assume that sub-trajectories are *local* i.e they could be as small as 12cm of total robot displacement. This comes from the known result in antenna array theory stating that a full AOA profile is attainable over a minimum array length of 2λ, which is on the order of 12cm of total robot displacement for 5Ghz WiFi.

$\chi_i(t)$ is the vector of all poses $\chi_i(t_k) = (R_i(t_k), p_i(t_k))$ for $t \in [t_k, \ldots, t_l]$, where $R_i(t_k) \in SO(3)$ is orientation, $p_i(t_k) \in \mathbb{R}^3$ is position. k is any timestep when the robot wants to initiate data collection for 3D SAR; i.e. to obtain relative AOA to any transmitting robots $j \in \mathcal{N}_i$ in its *neighborhood*. $\mathcal{N}_i$ includes all transmitting robots j for which robot i can atleast obtain ping packets (i.e. broadcasting at 5 kB/s over 3 seconds). Note that signal packets from all $j \in \mathcal{N}_i$ simultaneously collected over a single local trajectory $\chi_i(t)$, can be used to compute individual AOA profiles for *all* robots in parallel. A pose of robot i in $\hat{\chi}_i(t)$ at time t_k is represented as $\hat{\chi}_i(t_k) = (R_i(t_k)R_\epsilon(t_k), p_i(t_k) + p_\epsilon(t_k))$. Let $R_\epsilon(t)$ and $p_\epsilon(t)$ denote
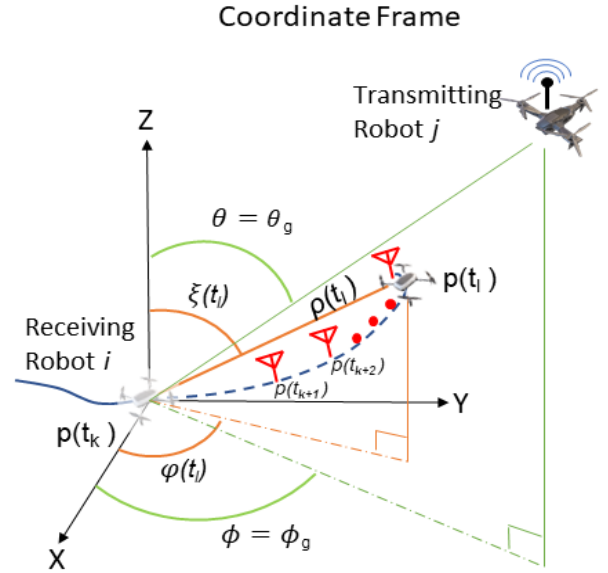

Figure 5. *Spherical coordinate system used by our system in receiving robot i's local frame of reference. Robot i uses M wireless signal measurements and its corresponding position estimates p(t) = (ρ,φ,ξ) from time t_k to t_l, l = k + M for each position (red antennas) to emulate M virtual antenna array elements and obtain relative angles φ (azimuth) and θ (elevation) to the signal transmitting robot j. True relative AOA (obtained from motion capture system) is denoted by (φ_g, θ_g).*

the accumulated error in estimated position and orientation from time t_0 (The very first timestep when robot start to move) to any time t_k.

We use $\hat{p}_i(t)$ to denote robot i's estimated position for a pose in $\hat{\chi}_i(t)$ i.e $\hat{p}_i(t) = p_i(t_k) + p_\epsilon(t_k)$. As our system can handle the motion of transmitting robots, let $\chi_{ij}(t_{k:l})$ denote the relative trajectory of robot i with respect to another robot $j \in \mathcal{N}_i$ over the time window from $t = t_k$ to $t = t_l$, calculated as $\chi_{ij}(t_{k:l}) = \chi_i(t_{k:l}) - \chi_j(t_{k:l})$. For brevity we denote this *relative* sub-trajectory over the time vector $[t_k, \ldots, t_l]$ as $\chi_{ij}(t)$ in the sequel. In Sec. 6 we show its validity even when the coordinate frames of robot are different.

3.3 A primer on Synthetic Aperture Radar (SAR).

An application of SAR over robot trajectories requires that a robot travel over some small local displacement (of at least 2λ) while taking several measurements $h_{ij}(t)$ of the wireless communication channel from its neighboring robots $j \in \mathcal{N}_i$. The ideal channel at time t is modeled following the common far-distance assumption when signal waves are assumed to be planar (Tse and Viswanath, 2005) :

$$h_{ij}(t) = \frac{1}{d_{ij}(t)} e^{\left(\frac{-2\pi\sqrt{-1}}{\lambda} d_{ij}(t)\right)} \quad (1)$$

where $d_{ij}(t)$ is the groundtruth distance between $p_i(t)$ and $p_j(t)$. Over its trajectory, the robot creates a history of packet-position tuples $< h_{ij}(t), p_i(t) >$, where each such

---

*A position (ρ, ϕ, θ) in spherical coordinates has corresponding Cartesian coordinates (x, y, z) as $(\rho \sin\theta \cos\phi, \rho \sin\theta \sin\phi, \rho \cos\theta)$.

tuple is essentially an emulation of omnidirectional "antenna element" in a virtual multi-antenna array. In the case of WiFi pings or thousands of packets can be transmitted at 5kB/s which is much lower than the lowest protocol rate of 6Mb/s, a large number of antennas can be emulated with very little communication overhead[†]. Thus using its local trajectory and transmitted signals from robot $j \in \mathcal{N}_i$, the wireless channel at robot i can be modeled using the multi-antenna array output observation model from (Vu et al., 2010) as:

$$\mathbf{Y_{ij}(t)} = [Y(t_k), \ldots, Y(t_l)]^T = \mathbf{a}(\theta, \phi)(\mathbf{t})\mathbf{h_{ij}(t)} + \mathbf{n(t)} \tag{2}$$

where $Y(t_k)$ is received signal at robot position $p_i(t_k)$, the total number of signal packets received is M, and $l = k + M$. The vector $\mathbf{a}(\theta, \phi)(\mathbf{t})$ is the *steering vector*, which is defined by the robot's local trajectory $\mathbf{\chi_i(t)}$ and thus dictates the *geometry* of arbitrary 3D antenna array. This steering vector is a function of the geometry of the antenna array (i.e. robot i's positions $p_i(t)$, $t \in [t_k, t_l]$) and the angle tuple (ϕ, θ) for transmitting robot $j \in \mathcal{N}_i$ (See Fig. 5):

$$\mathbf{a}(\theta, \phi)(\mathbf{t}) = e^{\left(\frac{2\pi\sqrt{-1}}{\lambda} f(p_i(t), \phi, \theta) \right)} \tag{3}$$

Here, λ is the signal wavelength and $\mathbf{n(t)}$ is a signal noise vector, assumed to be Gaussian, circular, independent and identically distributed, with a mean of zero and a covariance of $\sigma^2 I$, where I is the identity matrix of appropriate dimension. The wireless channel measurement at time t, $h_{ij}(t)$, which is a complex number capturing the phase and magnitude of the received signal, can be obtained using the *Channel State Information (CSI) Toolbox* (Halperin et al., 2011). $\mathbf{h_{ij}(t)} = [h_{ij}(t_k), \ldots, h_{ij}(t_l)]$ is thus known at the receiving robot.

Using direction finding algorithms like Bartlett or MUSIC from antenna array theory (Krim and Viberg, 1996), the AOA profile $F_{ij}(\phi, \theta)$ can be obtained by measuring the signal phase difference of each array element with respect to the first element at $p(t_k)$. We use the Bartlett estimator we get:

$$F_{ij}(\phi, \theta) = \left| \sum_{t=t_k}^{t_l} h_{ij}(t) \, a(\theta, \phi)(t) \right|^2 \tag{4}$$

$F_{ij}(\phi, \theta)$ thus refers to relative paths a WiFi signal traverses between a given pair of signal transmitting robot j and receiving robot i. Mathematically, it is a 2D matrix calculated for all possible incoming signal directions along azimuth and elevation (360 x 180). Thus, henceforth we refer to AOA_{max} as the strongest signal direction ($\hat{\phi}, \hat{\theta}$), or *the AOA peak corresponding to maximum magnitude path*, in the full AOA profile $F_{ij}(\phi, \theta)$.

A reference to all notations and terminology can be found in Appendix section B. Next we formulate the problems that are addressed in this paper.

4 Problem Formulation

This paper aims to enable robots in a team to infer relative spatial directions, i.e an Angle-of-Arrival (AOA)

profile $F_{ij}(\phi, \theta)$ to others in its neighborhood, based on received communication signals between them. In doing so, we aim to develop an "inter-robot sensor" for robots to obtain relative directional information about each other by analyzing existing *communication packets* in the network. We leverage off-the-shelf WiFi modules for this purpose. Specifically, our goal is to find $F_{ij}(\phi, \theta)$. Of particular interest is finding the maximum magnitude path AOA_{max}, between the robots referred to as the *azimuth angle ϕ* and *elevation angle θ* to a neighboring transmitting robot (see Fig. 5)[‡]. Our system uses an approach akin to Synthetic Aperture Radar for this purpose. Key challenges for applying SAR-based methods to heterogeneous robot systems that we aim to address in this paper are:

1. **Mobility:** Developing a framework to support AOA profile generation where both the transmitting and receiving robots are simultaneously mobile along arbitrary 2D or 3D trajectories during data capture. This is a commonly encountered scenario in multi-robot teams that must be accounted for in our SAR formulation in order to allow for continuous AOA sensing capabilities amongst the robots.

2. **Trajectory geometry:** Characterizing *informativeness*, or the impact of *robot trajectories* on the sensitivity of the resulting phase measurements and the resulting $F_{ij}(\phi, \theta)$. We do so by studying the impact of *antenna array geometry* on the accuracy of the AOA_{max} which is not readily known for arbitrary shapes such as those generated by arbitrary robot trajectories.

3. **Estimation Noise:** Analyzing the effect of trajectory estimation error on $F_{ij}(\phi, \theta)$. In real robotic systems it is possible to obtain local robot displacement estimates using various tools such as inertial measurements and VIO, however it is well known that these estimates are subject to noise. Thus the impact of this estimation noise on the accuracy of the resulting AOA_{max} estimation must be quantified.

4.1 Simultaneous robot motion

As many previous approaches that use SAR to obtain AOA_{max} require transmitting robots to remain static during the period of data collection (Wang et al., 2019; Wang and Katabi, 2013; Karanam et al., 2018), they are not feasible for applications that require continuous mobility of all the robots. Additionally, they do not account for arbitrary motion of robots in 2D and 3D. This necessitates that our system account for motion of both signal transmitting and receiving robots and we refer to this as the *moving ends* problem.

Problem 1. Moving ends problem. *Given WiFi signal receiving robot i's local trajectory from position $p_i(t_k)$) to $p_i(t_l)$) and transmitting robot j's, $j \in \mathcal{N}_i$, local trajectory*

[†]The total communication overhead incurred by our system is around 15 Kb

[‡]We note that in some cases the strongest signal path may not be the direct path which might be attenuated due to absorption or reflection of signals. However in this case there exist many methods for inferring the direct path (Kumar et al., 2014a; Kotaru et al., 2015). In this paper we do not address the problem of finding the direct path from $F_{ij}(\phi, \theta)$ and rather refer the reader to relevant references for the solution to this problem.
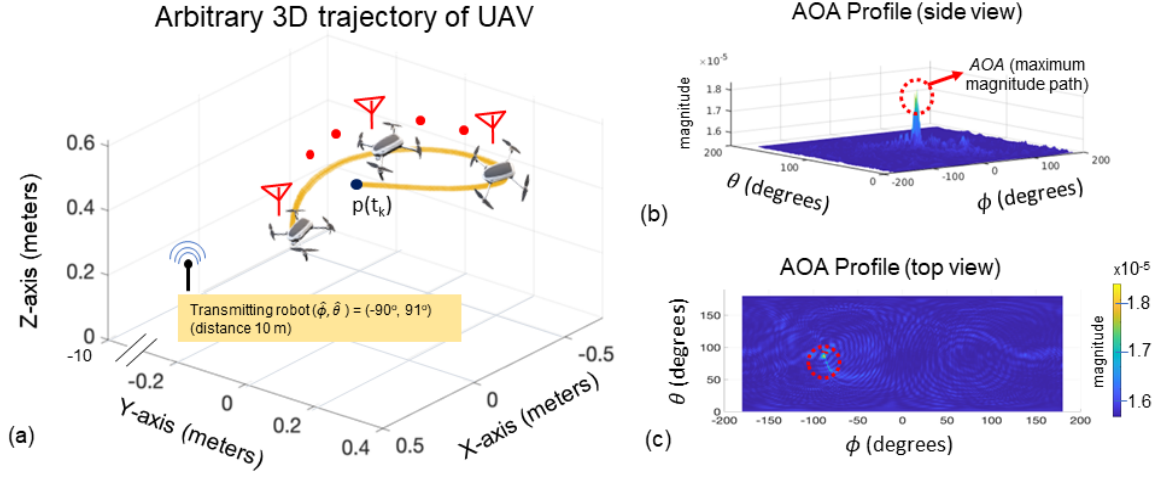
Figure 6. *(a) Shows the arbitrary 3D groundtruth trajectory of a signal receiving UAV from our hardware experiments, the start position $p(t_k)$ indicated by a blue circle. (b) Corresponding AOA profile obtained for the trajectory using our formulation shows the AOA (strongest signal direction) which corresponds to the relative direction of the transmitting robot (indicated by black antenna) located at true AOA $(\phi_g, \theta_g) = (-90°, 91°)$ and at a distance of 10 m in line-of-sight. Our system returns AOA $(\hat{\phi}, \hat{\theta}) = (-91.5°, 92.5°)$.*

from position $p_j(t_k)$) to $p_j(t_l)$), obtain $F_{ij}(\theta, \phi)$ where $a(\phi, \theta)(t)$ characterizes robot i's relative trajectory $\chi_{ij}(t)$ with respect to robot j.

We first formulate the SAR based solution in Sec. 5 for obtaining $F_{ij}(\phi, \theta)$ from arbitrary 3D motion of receiving robot, by applying the concepts from antenna array theory (Fig. 6). In Sec. 6 we use this formulation of 3D SAR for a static transmitting robot to solve the moving ends problem.

4.2 Information gain from trajectory geometry

Our formulation can leverage different robot trajectory shapes in 2D and 3D to emulate virtual antenna arrays of varying geometry. It is well known that an array's geometry affects its sensitivity to differentiate phases of an arriving signal from different source locations (Manikas, 2004). For the case of interest in this paper where robots can operate in the full 3D space (not just 2.5D), sensitivity of the array and the ability to estimate AOA_{max} consistently independent of source location, is of utmost importance. For the purposes of characterizing the sensitivity of a particular antenna array geometry, the Cramer Rao Bound (CRB) is often employed (Gazzah and Marcos, 2006). The Cramer Rao Bound is a lower bound on the variance of the AOA_{max} estimation resulting from a particular antenna array geometry and is given by (dropping t and subscript i,j for brevity):

$$CRB = \begin{bmatrix} C_{\theta\theta} & C_{\theta\phi} \\ C_{\phi\phi} & C_{\phi\phi} \end{bmatrix}$$

$$= \frac{\sigma^2}{2\mathbf{h}^H\mathbf{h}} \underbrace{\begin{bmatrix} Re(\frac{\partial a^H(\theta,\phi)}{\partial\theta}\frac{\partial a(\theta,\phi)}{\partial\theta}) & Re(\frac{\partial a^H(\theta,\phi)}{\partial\theta}\frac{\partial a(\theta,\phi)}{\partial\phi}) \\ Re(\frac{\partial a^H(\theta,\phi)}{\partial\phi}\frac{\partial a(\theta,\phi)}{\partial\theta}) & Re(\frac{\partial a^H(\theta,\phi)}{\partial\phi}\frac{\partial a(\theta,\phi)}{\partial\phi}) \end{bmatrix}}_{FIM}^{-1}$$

$$(5)$$

for a particular source direction indicated by its azimuth angle θ and elevation angle ϕ. Here σ^2 is the variance in noise of the wireless signal. FIM is the *Fisher Information Matrix* which measures the amount of information that the

geometry of the antenna array (captured via $\mathbf{a}(\theta, \phi)(\mathbf{t})$ i.e the steering vector) provides on $F_{ij}(\phi, \theta)$. Since in our problem formulation the geometry of the virtual antenna array is dictated by the trajectory of the receiving robot, we define the *informativeness* of a trajectory using the CRB as follows.

Definition 1 (Informativeness) : We say that a trajectory is more *informative* than another if it permits a smaller variance in AOA_{max} as dictated by the Cramer Rao Bound (CRB).

Thus, the second problem that we wish to tackle in this paper is the characterization of the informativeness for different robot trajectories; i.e. the effectiveness of our AOA_{max} estimation capabilities as a function of the trajectory traversed by a robot as it is receiving communication packets from its neighbors.

Problem 2. Informativeness. *We wish to derive the formulation for the Cramer-Rao Bound (cf. Eqn. (5)) in the θ and φ directions for arbitrary 3D robot trajectories, thereby characterizing the* informativeness *of different robot trajectories.*

Sec. 7.1 details the theoretical development our CRB analysis for three types of common robot trajectories: 3D helix, 2D planar circular and 2D linear. Our experimental analysis further shows that the insights garnered for these trajectory types generalize to overall trends in arbitrary 2D and 3D robot trajectories.

4.3 Impact of trajectory estimation error

Although our approach is independent of how such robot trajectories are obtained, in order to make our system native to robotic platforms, our goal is to leverage trajectory estimates from on-board sensors (e.g VIO camera). Therefore, the third problem that we address in this paper is to characterize, both analytically and experimentally, the impact of the receiving robot's trajectory estimation error on its generated $F_{ij}(\phi, \theta)$. In this paper, we use robot trajectories of the following two types to test our system's performance:

- *Groundtruth trajectory*: obtained using position estimates from motion capture system denoted by $p(t)$ at time t.
- *Tracking camera trajectory*: obtained using position estimates from Intel Realsense T265 tracking camera. This out-of-the-box camera runs a visual SLAM algorithm which provides pose estimates at 200 Hz. We denote the estimated position at time t as $\hat{p}(t)$.

Using trajectories from tracking camera introduces error in $F_{ij}(\phi, \theta)$ on account of noisy trajectory estimation. A commonly used metric to quantify error in trajectory estimation is Absolute Trajectory Error (Sturm et al., 2012; Choudhary et al., 2017b), given by the equation below

$$ATE_{\text{trans}} = \left(\frac{1}{n} \sum_{t=t_k}^{t_l} ||p(t) - \hat{p}(t)||^2 \right)^{\frac{1}{2}} \quad (6)$$

As ours is a relative direction finding system that uses spherical coordinates, we use an angular drift metric (Camposeco and Pollefeys, 2015) for our theoretical analysis to quantify the error in trajectory[§]. This is given as:

Definition 2 (Angular drift) : For every groundtruth position in a robot trajectory $p(t) = (\rho, \varphi, \xi)$, we get an estimated position $\hat{p}(t) = ((\rho - \kappa_\rho, \varphi - \kappa_\phi, \xi - \kappa_\theta))$, whenever κ_ϕ, κ_θ are constant or varying angular error and κ_ρ, we say that the trajectory has an angular drift.

Since a robot's trajectory is used to generate the full $F_{ij}(\phi, \theta)$ (cf. Eqn. 4), an error in trajectory estimation will result in an error in AOA_{max} calculation between two robots. We define this error to be *AOA Estimation Error*.

Definition 3 (AOA error) : We define error in AOA as $\phi_g - \hat{\phi}$ in azimuth and $\theta_g - \hat{\theta}$ in elevation, where (ϕ_g, θ_g) is the true AOA to the signal transmitting robot and $(\hat{\phi}, \hat{\theta})$ is the estimated *AOA* obtained by our system.

We use L2 norm between estimated AOA_{max} and true AOA, as an error metric given by the equation:

$$AOA_{Error} = \sqrt{(\phi_g - \hat{\phi})^2 + (\theta_g - \hat{\theta})^2} \quad (7)$$

Thus we can now define our problem of characterizing the impact of trajectory estimation error on AOA error as:

Problem 3. Impact of trajectory estimation error. *For nonzero trajectory estimation error ATE_{trans}, we wish to characterize the effect of angular drift $\kappa_\phi > 0$, $\kappa_\theta > 0$ on the error, AOA_{Error} in Eqn. (7), in our measured AOA_{max}.*

We note that in practice AOA error can arise from simultaneous impact of many factors, including insufficient informativeness of robot trajectories, artifacts from AOA estimation algorithms or errors in robot position estimation, and channel noise or unaccounted for phase shifts due to *Carrier Frequency Offset* (CFO) or mobility of robot platforms (i.e. the *moving ends* problem). In this paper we analyze the effects of these sources of error on $F_{ij}(\phi, \theta)$ independently.

Finally, we aim to extensively validate our system's accuracy and performance on real robotic platforms in 2D

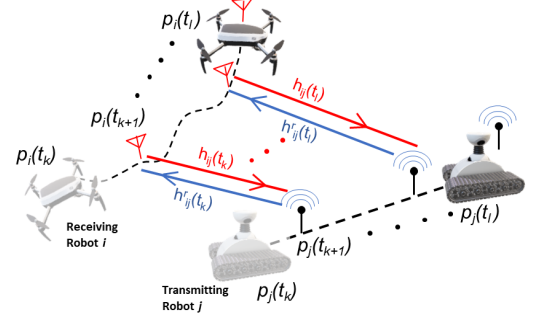Cancelling CFO using Forward Reverse Approach

Figure 7. *Schematic representation of forward channel (from robot i to robot j) and reverse channel (from robot j to robot i). This enables our system to cancel the Carrier Frequency Offset (CFO).*

and 3D space. In Sec. 9, we evaluate the utility of our system for a dynamic rendezvous experiment based different trajectory geometries generated during navigation in an unmapped environment in presence of moving ends and occlusions in the environment.

We summarize key assumptions used throughout the paper:

Assumptions (Common paper assumptions) .

1. Robots know the true *North* and true *Down* direction using on-board sensor like magnetometer and gyroscope/gravity sensor respectively.
2. Each robot has the same global clock to match forward-reverse channel packets based on timestamps used subsequently for canceling the effects of *carrier frequency offset* (CFO).
3. All AOA measurements are taken with respect to the initial position $p_i(t_k)$ of robot i in its local frame.

In the next section we derive our general formulation for 3D arbitrary trajectory SAR and demonstrate how a moving robot can use it for obtaining relative AOA_{max} to a static transmitting robot. Following this, we show how our formulation can be extended to address the full mobility case, i.e. the moving ends problem.

5 SAR for Arbitrary Trajectories

Trajectory estimation methods generally result in substantial orientation and position errors $R_\epsilon(t)$ and $p_\epsilon(t)$ for longer trajectories and without loop closures (Nobre et al., 2017). We use local sub-trajectory estimate $\hat{\chi_i}(\mathbf{t})$ for receiving robot i over M robot positions $p_i(t_k), \ldots, p_i(t_l)$, $l = k + M$, in order to obtain the AOA profile $F_{ij}(\phi, \theta)$ (e.g. Fig. 6) for *arbitrary motion* in 2D and 3D. In practice M can be about 200 packets collected over a few seconds and the length of the local sub-trajectory should be $\geq 2\lambda$. We define the residual error $\epsilon(t)$ for any pose in $\hat{\chi_i}(\mathbf{t})$ as follows:

Definition 4 (Residual Error) : Given error $p_\epsilon(t_k)$ in position $p(t_k)$ for the first pose $\hat{\chi_i(t_k)}$ in $\hat{\chi_i}(\mathbf{t})$, for any time $t \in$

[§]For empirical evaluation, the corresponding ATE_{trans} is calculated in Cartesian coordinates for simplicity.

$[t_k, \ldots, t_l]$, the residual error is given as $\epsilon(t) = p_\epsilon(t) - p_\epsilon(t_k)$.

As stated in our assumptions all measurements are with respect to $p_i(t_k)$. Thus, a position $p_i(t_u)$ at timestep t_u in the sub-trajectory becomes:

$$p(t_{uk}) + \epsilon(t_u) = p(t_u) - p(t_k) + p_\epsilon(t_u) - p_\epsilon(t_k)$$

where $p_i(t_{uk})$ is position $p_i(t_u)$ relative to the position at time $p_i(t_k)$ and $\epsilon(t_u)$ is the residual error. Note that our system is not impacted by orientation errors since it uses an omnidirectional antenna. In other words, our system is only impacted by the accumulation of residual errors (and trajectory geometry as discussed in Sec. 7). For the rest of the paper any position $p_i(t_u)$ for a robot i is implicitly assumed to be $p_i(t_{uk})$ for brevity.

Given a perfect trajectory estimation $\chi_i(\mathbf{t})$, the errors terms can be set to zero as in the case of using a motion capture system. We redefine the steering vector $\mathbf{a}(\theta, \phi)(\mathbf{t})$ from Eqn. 3 in spherical coordinates as follows: (dropping the notation t and subscript i for brevity)

$$\mathbf{a}(\theta, \phi) = \begin{bmatrix} e^{\left(\frac{2\pi \rho_k \sqrt{-1}}{\lambda} \sin\theta \sin\xi_k \cos(\phi - \varphi_k) + \cos\xi_k \cos\theta \right)} \\ \vdots \\ e^{\left(\frac{2\pi \rho_l \sqrt{-1}}{\lambda} \sin\theta \sin\xi_l \cos(\phi - \varphi_l) + \cos\xi_l \cos\theta \right)} \end{bmatrix} \quad (8)$$

As $\mathbf{h_{ij}}(\mathbf{t})$ is a vector of signal measurements at each position in $\chi_i(\mathbf{t})$, the steering vector enables calculating the phase difference between antenna positions in virtual antenna array, which then can be used with AOA calculation algorithms like Bartlett to obtain $F_{ij}(\phi, \theta)$ for pair of communicating robots i, j.

However, since the wireless signal transmitter and receiver are separate Wi-Fi devices (i.e. different robots in a team), the signal oscillators in those devices have different frequencies with offset Δ_f. This leads to time-varying phase offset in the signal phase called *Carrier Frequency Offset* (CFO), leading to erroneous measurements. Following the development in (Gil et al., 2015a), we use *channel reciprocity* to rectify this. Channel reciprocity states that i) ratio of forward and reverse channel (See Fig. 7) is constant over time i.e $h_{ij}(t)/h_{ij}^r(t) = \kappa_h$, where κ_h is constant because the forward and backward channel would be received almost simultaneously and ii) The frequency offset in reverse direction is the negative for offset in forward direction i.e $-\Delta_f$. Hence, the observed forward and reverse channels, $\hat{h}_{ij}(t)$ and $\hat{h}_{ij}^r(t)$ respectively, that are affected by frequency offset Δ_f (and $-\Delta_f$), are given as follows for any position $p_i(t)$ in the sub-trajectory:

$$\hat{h}_{ij}(t) = h_{ij}(t)e^{-2\pi\Delta_f(t-t_k)} \quad (9)$$

$$\hat{h}_{ij}^r(t) = h_{ij}^r(t)e^{2\pi\Delta_f(t-t_k)} \quad (10)$$

We then obtain the rectified wireless channel $h_{ij}(t)$ as the product of observed forward channel $\hat{h}_{ij}(t)$ and reverse channel $\hat{h}_{ij}^r(t)$:

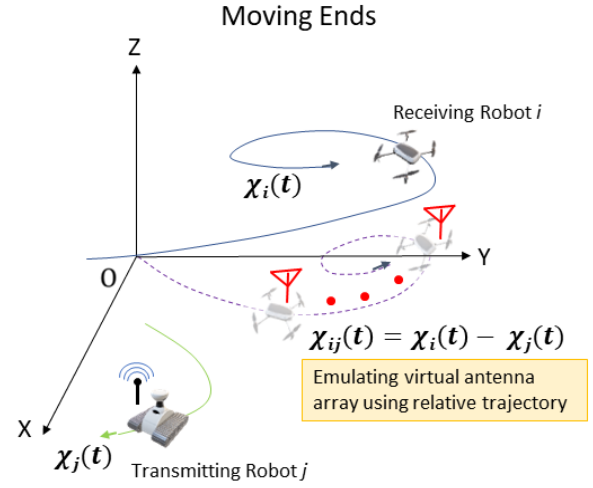$$h_{ij}(t) = \sqrt{\hat{h}_{ij}(t)\,\hat{h}_{ij}^r(t)/\kappa_h} \quad (11)$$

Figure 8. *Schematic showing relative trajectory $\chi_{ij}(t)$ of the UAV with respect to moving transmitting ground robot j. $\chi_i(t)$ and $\chi_j(t)$ denote the actual trajectories of the robot i (emulating virtual antenna array) and robot j.*

Rewriting Eqn. 4 and dropping κ_h as it is a constant scaling factor, we get the AOA profile of transmitting robot j for a receiving robot i as follows:

$$F_{ij}(\phi, \theta) = \left| \sum_{t=t_k}^{t_l} \hat{h}_{ij}(t)\, \hat{h}_{rij}(t)\, \mathbf{a}(\theta, \phi)(t) \right|^2 \quad (12)$$

This formulation provides the solution to the problem of measuring $F_{ij}(\phi, \theta)$ over arbitrary robot trajectories in 3D space for the static transmitting robot case. Thus by allowing robots to emulate an antenna array in full 3D space over its local trajectory, we obtain maximum magnitude signal path AOA_{max} to a static neighboring robot. We address the more general problem of simultaneous mobility of both the transmitting and receiving robot, the *moving ends problem*, in the subsequent section.

6 Moving Ends Formulation

In this section we generalize our framework from Sec. 5 to accommodate the case where both receiving and transmitting robots are moving simultaneously during the data collection phase. This case is particularly challenging since not accounting for relative displacements between agents can greatly impact the resulting signal phase measurements – leading to errors in the generated AOA profile $F_{ij}(\phi, \theta)$. Here, we show that a receiving robot i can calculate $F_{ij}(\phi, \theta)$ to a moving transmitting robot j by using the relative trajectory obtained from it's own and robot j's local trajectory estimates – namely, by using $\chi_{ij}(\mathbf{t})$ as the steering vector (Fig. 8). One clear difficulty in computing $\chi_{ij}(\mathbf{t})$ is that robot i and robot j *do not share a common coordinate reference frame* in the most general case. However, we begin the development of this section assuming the availability of a shared reference frame and then generalize to the case of different local coordinate frames between agents.

For the time being, let us assume that the robots have a common frame of reference (an assumption that we later relax). Thus, any position $p_{ij}(t)$ for pose $\chi_{ij}(t)$ in robot i's
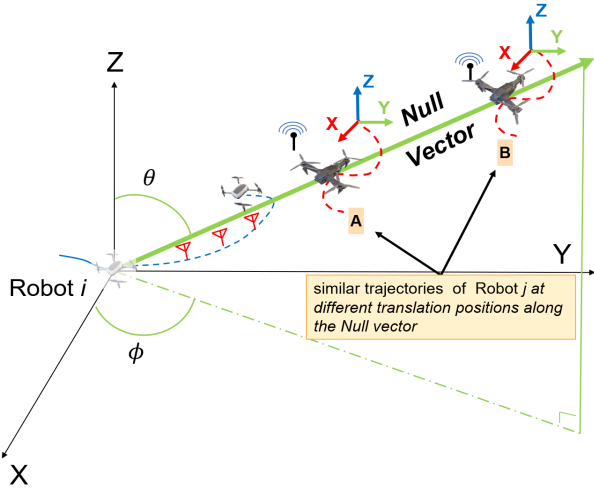
Figure 9. *Schematic representation of the Null vector of robot i (performing 3D SAR) for Angle-of-Arrival (ϕ,θ). Rotation offset between any robot $j \in \mathcal{N}_i$ and robot i's local coordinate frames can be removed by aligning the robots to true NORTH and DOWN direction (using on-board sensors like magnetometer and gyroscope/gravity sensor). At any position on Null vector (e.g position A and B), robot j will lead to same phase change in WiFi signal, if the trajectory geometry is same (dotted red line).*

relative trajectory $\chi_{ij}(\mathbf{t})$ for $t \in [t_k, \dots, t_l]$ is given as:

$$p_{ij}(t) = (p_i(t) - p_j(t)) - (p_i(t_k) - p_j(t_k)) \quad (13)$$

This is because all poses in the local trajectory $\chi_i(\mathbf{t})$ are relative to the starting pose $\chi_i(t_k)$ in the trajectory for any robot i. Essentially, as our method uses the 'local sub-trajectory' with respect to the pose at time t_k for any given robot, the relative poses obtained as per Eqn. (13) can thus be applied to obtain steering vector. $F_{ij}(\phi, \theta)$ can then be calculated with the same 3D SAR formulation developed in Sec. 5.

In reality however, we do not have access to a global frame of reference and the local coordinate frames of the robots will have a rotation and translation drifting offset compared to global frame, thus making the computation of a relative trajectory difficult to obtain. We introduce the following lemma which shows how a robot can obtain $F_{ij}(\phi, \theta)$ in the presence of these offsets. We first define the concept of a *null vector* which captures the translation independent character of wireless signal phase measurements.

Definition 5 (Null Vector) : We define the *Null Vector* of a receiving robot i as a vector along a specific angle-of-arrival from it's start position $p_i(t_k)$. A transmitting robot j at any position on this *Null Vector* and performing the same trajectory motion will lead to same change in *phase* of the wireless signal intercepted by robot i (see Fig. 9).

This is due to the fact that channel phase measurements are independent of the distance between a signal transmitter and receiver (for a detailed discussion, refer (Ioannides and Balanis, 2005)). Thus, using the concept of a *Null vector* we show that robots sharing a common North vector and gravity vector is sufficient to compute $\chi_{ij}(\mathbf{t})$ as needed by our steering vector in Eqn. (8).

Lemma 1. *Given trajectories of two robots i and $j \in \mathcal{N}_i$, each in their own local frame of reference with rotation offset*

$\tilde{R}_i$, $\tilde{R}_j$ *with respect to a shared North vector, and a shared gravity vector and translation offset $\tilde{t}_{ij}$ with respect to each other, robot i can calculate relative AOA_{max} to robot j by correcting for rotation offset and ignoring the translation offset.*

Proof: As stated in our assumptions in Sec. 4, on-board sensors like magnetometer and gyroscope/gravity sensor can be used to rotate $\chi_i(\mathbf{t})$ of a robot i towards true *North* and *Down* by applying a rotation matrix, i.e $\tilde{\chi}_i(\mathbf{t}) = \tilde{R}_i\chi_i(\mathbf{t})$. Similarly any robot $j \in \mathcal{N}_i$ can align its coordinate frame such that $\tilde{\chi}_j(\mathbf{t}) = \tilde{R}_j\chi_j(\mathbf{t})$. Following Defn. (5), a robot j at a true AOA of angle of (ϕ,θ) to robot i will give similar *AOA* using our approach as long as it's anywhere on the *Null Vector* and performing same motion (Fig. 9). The relative trajectory can thus be obtained as $\chi_{ij}(\mathbf{t}) = \tilde{\chi}_i(\mathbf{t}) - \tilde{\chi}_j(\mathbf{t})$, since the presence of a translation offset $\tilde{t}_{ij}$ does not impact AOA_{max} calculation and one can use Eqn. (13) to compute the steering vector. We validate our approach in hardware experiment (Fig. 13), demonstrating our ability to compute $F_ij(\phi, \theta)$ for this moving ends problem in the Results Section of this paper (Sec. 8). As stated in our assumptions, the relative AOA is always computed with respect to position $p_i(t_k)$ of receiving robot i. Therefore we assume that robots are far enough away from each other such that local motions (which could be as small as 12cm when WiFi is used) will not significantly change their true relative AOA.

In the next section we analyze the impact of different trajectory shapes on $F_{ij}(\phi, \theta)$, i.e. we characterize trajectory *informativeness*. We also characterize the effect of errors in trajectory estimation on *AOA*.

7 Analysis of Trajectory Impact on Relative AOA Measurements

We establish theoretical performance bounds of our system as they relate to the AOA profile, $F_{ij}(\phi, \theta)$, accuracy. We do so by characterizing the effect of robot trajectories on the resulting accuracy of obtained AOA_{max} measurements that correspond to strongest signal direction, which is the direct signal path in our case. Two major factors that we analyze are the impact of *trajectory geometry* and the impact of *trajectory estimation errors* on the resulting AOA_{max} accuracy. Along these lines, in this section we independently analyzing the following factors:

1. **Trajectory geometry (2D, 3D)**: To analyze the system performance due to variations in trajectory geometry in ideal conditions, we formulate the Cramer-Rao bound for a *3D helix* as well as the two special cases of *Planar Curve* and *Linear* trajectories in Sec. 7.1. Our analysis shows that 3D trajectories lead to generally lower variance (higher *informativeness*) in $F_{ij}(\phi, \theta)$ compared to 2D trajectories.

2. **Trajectory estimation errors**: We analyze the performance of our system in the presence of both constant and varying position estimation error in the trajectory. We derive the mathematical relation between position estimation error and error in the $F_{ij}(\phi, \theta)$ in Sec. 7.2.

Although for the purposes of analysis we analyze these factors separately, in reality all of these factors will act

simultaneously to impact the accuracy of the resulting $F_{ij}(\phi, \theta)$. Our extensive empirical analyses from hardware experiments include simultaneous impact of both factors however, and demonstrates agreement with all analytical results presented in this paper.

7.1 Cramer Rao Bound for different trajectory geometries

Here, we consider the impact of the robots' trajectory shape on *AOA* estimation. Our main tool of analysis here will be the Cramer Rao Bound (CRB) which provides a lower bound on the variance of the AOA_{max} estimation for a given trajectory shape as captured by the steering vector $\mathbf{a}(\phi, \theta)(\mathbf{t})$ (cf. Eqn. (8)). This variance is inversely proportional to the *Informativeness* of the trajectory such that a lower variance indicates higher informativeness for a given trajectory shape (cf. Defn. 1). We note that the CRB is a function of source location at a given (ϕ, θ). In other words, the variance of the resulting AOA_{max} estimate is a function of the different relative directions between the transmitting and receiving robots. Intuitively, depending on the shape of the antenna array (dictated in our case by the receiving robot's trajectory), the phase differences in the received signal will be easier or harder to discern. In this section we analyze this discerning capability of different trajectories via the CRB. Specifically, in this section we develop a closed-form formulation of the CRB as a function of both trajectory as given by $\mathbf{a}(\phi, \theta)(\mathbf{t})$, and relative direction of the transmitting robot i.e (ϕ, θ).

We start by deriving the general form of the CRB for arbitrary robot trajectories. Given that $\mathbf{h_{ij}(t)}$ is complex, deterministic, and known at the receiver robot, it is clear from Eqn. 2 that output model $\mathbf{Y(t)}$ satisfies the *Conditional observation model*; i.e. it is multivariate Gaussian with mean $\mathbf{a}(\theta, \phi)(\mathbf{t}) \, \mathbf{h_{ij}(t)}$ and variance $\sigma^2 I$ (Vu et al., 2011). Thus, the expression for the CRB for an arbitrary 3D geometry array can be found in (Vu et al., 2010) as given in Eqn. 5 (dropping the notation t and subscript i, j for brevity):

$$\text{CRB} = \frac{\sigma^2}{2\mathbf{h}^H \mathbf{h}} \times$$

$$\underbrace{\begin{bmatrix} \underbrace{Re(\frac{\partial \mathbf{a}^H(\theta, \phi)}{\partial \theta} \frac{\partial \mathbf{a}(\theta, \phi)}{\partial \theta})}_{\mathbf{A}} & \underbrace{Re(\frac{\partial \mathbf{a}^H(\theta, \phi)}{\partial \theta} \frac{\partial \mathbf{a}(\theta, \phi)}{\partial \phi})}_{\mathbf{C}} \\ \underbrace{Re(\frac{\partial \mathbf{a}^H(\theta, \phi)}{\partial \phi} \frac{\partial \mathbf{a}(\theta, \phi)}{\partial \theta})}_{\mathbf{C}} & \underbrace{Re(\frac{\partial \mathbf{a}^H(\theta, \phi)}{\partial \phi} \frac{\partial \mathbf{a}(\theta, \phi)}{\partial \phi})}_{\mathbf{B}} \end{bmatrix}^{-1}}_{FIM}$$

where $\mathbf{h}^H \mathbf{h} = \|h\|^2$ is signal magnitude, and Re stands for real number. It is also inversely proportional to the FIM (Fisher Information Matrix), as indicated above. Following the development in (Vu et al., 2010, Sec. 6), derivatives of the uth element of the steering vector with M total elements are given as:

$$\frac{\partial a_u(\theta, \phi)}{\partial \theta} =$$
$$\frac{2\pi \rho_u \Upsilon_u \sqrt{-1}}{\lambda} (\cos\theta \sin\xi_u \cos(\phi - \varphi_u) - \cos\xi_u \sin\theta)$$

$$\frac{\partial a_u(\theta, \phi)}{\partial \phi} = -\frac{2\pi \rho_u \Upsilon_u \sqrt{-1}}{\lambda} (\sin\theta \sin\xi_u \sin(\phi - \varphi_u))$$

where

$$\Upsilon_u = e^{\frac{2\pi \rho_u \sqrt{-1}}{\lambda} (\sin\theta \sin\xi_u \cos(\phi - \varphi_u) + \cos\xi_u \cos\theta)}$$

After some simplification the partial derivative terms in the FIM become:

$$\mathbf{A} = \frac{\partial \mathbf{a}^H(\theta, \phi) \partial \mathbf{a}(\theta, \phi)}{\partial \theta \partial \theta} =$$
$$\sum_{u=1}^{M} \frac{4\pi^2 \rho_u^2}{\lambda^2} (\cos\theta \sin\xi_u \cos(\phi - \varphi_u) - \cos\xi_u \sin\theta)^2$$

and:

$$\mathbf{B} = \frac{\partial \mathbf{a}^H(\theta, \phi) \partial \mathbf{a}(\theta, \phi)}{\partial \phi \partial \phi} =$$
$$\sum_{u=1}^{M} \frac{4\pi^2 \rho_u^2}{\lambda^2} (\sin\theta \sin\xi_u \sin(\phi - \varphi_u))^2$$

and finally:

$$\mathbf{C} = \frac{\partial \mathbf{a}^H(\theta, \phi) \partial \mathbf{a}(\theta, \phi)}{\partial \phi \partial \theta} =$$
$$\sum_{u=1}^{M} \frac{4\pi^2 \rho_u^2}{\lambda^2} (\cos\theta \sin\xi_u \cos(\phi - \varphi_u) - \cos\xi_u \sin\theta)$$
$$\times (\sin\theta \sin\xi_u \sin(\phi - \varphi_u))$$

Taking the determinant of the FIM, we arrive at the general form for the CRB in each the θ and ϕ directions:

$$CRB_\theta = \frac{\sigma^2}{2\|h\|^2 \, Det(FIM)\mathbf{A}}$$
$$CRB_\phi = \frac{\sigma^2}{2\|h\|^2 \, Det(FIM)\mathbf{B}} \tag{14}$$

where σ^2 is the variance of our noise and $\|h\|$ is the magnitude of our signal, that is, $\frac{\sigma^2}{2\|h\|^2} = \frac{1}{\text{SNR}}$, where SNR is the signal to noise ratio.

In the following sections, we include specific forms of the CRBs for three types of symmetrical trajectory geometries that can be obtained on robot platforms - 2D linear, 2D curved and a 3D helix, to obtain in-depth insights on how their corresponding CRB values impact relative AOA. In section 8.3 we show that these insights generalize well for arbitrary shaped 2D and 3D trajectories. Detailed derivations of CRB for these trajectories can be found in Appendix section A.

7.1.1 *Analysis of special geometries.*

(a) [3D spherical helix]. We begin by considering the case of a 3D spherical helix trajectory to build intuition on the impact of 3D trajectories on the CRB. For such a trajectory, its spherical coordinates are given by (dropping t and subscript i for brevity):

$$\xi_u = \tau, \quad \varphi_u = c\tau, \quad \rho_u = r$$
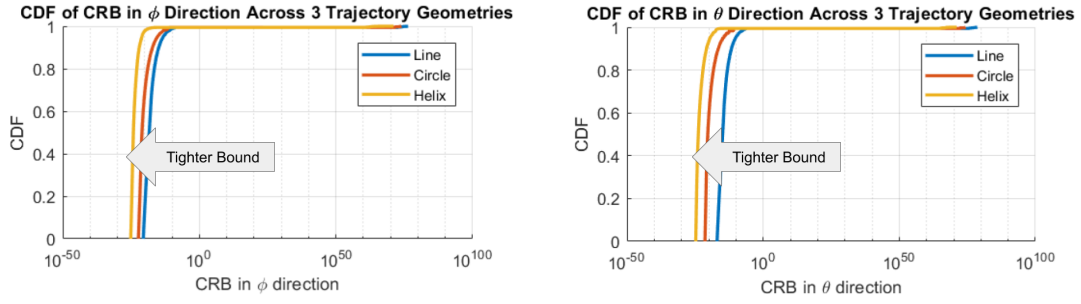
(a) *Cramer-Rao Bound for a simulated receiving robot trajectory in ϕ (azimuth) direction*

(b) *Cramer-Rao Bound for a simulated receiving robot trajectory in θ (elevation) direction*

Figure 10. *CDF plot showing the effect of trajectory shape on Cramer-Rao Bound in the (a) ϕ direction and (b) θ direction for a receiving robot's simulated trajectory of fixed length, from 129600 simulated locations of transmitting robot that are uniformly distributed in 3D space. We see that 3D trajectory (helix) has a tighter bound compared to 2D trajectories (circle and line). Cumulative result from hardware experiments (Fig. 15) demonstrates that indeed the informativeness calculated for each trajectory (inverse of the CRB) successfully captures the improved performance in AOA estimation for 3D versus 2D trajectories.*

for a spherical helix of radius r, spiral climb rate of c, and parameterization $\tau \in [0, 2\pi]$. We assume that each antenna element u is uniformly spaced along the helix so that $\tau = \{0, \Delta, 2\Delta, \ldots, (M-1)\Delta\}$ where $\Delta = \frac{2\pi}{M}$. Further, we assume a climb rate $c = 1$ for a simplification of our closed form, though any constant can be similarly substituted before integration. So for our 3D spherical helical trajectory, our CRB terms become:

$$\mathbf{A} = -\frac{\pi^2 r^2 \left(\cos^2(\theta)\cos(2\phi) + \cos(2\theta) - 3\right)}{\lambda^2}$$

$$\mathbf{B} = \frac{\pi^3 r^2 \sin^2(\theta)(\cos(2\phi) + 2)}{\lambda^2}$$

$$\mathbf{C} = \frac{2\pi^3 r^2 \sin(\theta)\cos(\theta)\sin(\phi)\cos(\phi)}{\lambda^2}.$$

The Fisher Information for θ and ϕ are given by $\frac{2\|h\|^2}{\sigma^2}\mathbf{A}$ and $\frac{2\|h\|^2}{\sigma^2}\mathbf{B}$ respectively (Vu et al., 2011). We calculate the determinant of FIM as follows:

$$\mathbf{Det}(\text{FIM}) =$$

$$\frac{\pi^5 r^4}{8\lambda^4}\sin^2(\theta)(8\cos(2(\theta - \phi)) + 8\cos(2(\theta + \phi))$$
$$+ \pi\cos(2(\theta + 2\phi)) + \cos(2(\theta + 2\phi))$$
$$+ (1 + \pi)\cos(2(\theta - 2\phi))$$
$$- 2(\pi - 9)\cos(2\theta) - 16\cos(2\phi) + 2\pi\cos(4\phi)$$
$$+ 2\cos(4\phi) - 2\pi + 50)$$

Substituting $\mathbf{A}$, $\mathbf{B}$, and $\mathbf{Det}$(FIM) into Eqn. 14 thus gives the corresponding closed form equation of the CRB for a spherical helix (Derivation in Appendix A (I)).

(b) $z = 0$ [Planar circular trajectory]. For $z = 0$ the helix is a circle of radius r and the CRB equations should be the same as a circular planar curve. For this case we have (dropping t and subscript i for brevity):

$$\xi_u = \tau, \quad \rho_u = r, \quad \varphi_u = \cos^{-1}(0) = \pi/2$$

The CRB equations reduce to

$$\mathbf{A} = \frac{2\pi^2 r^2}{\lambda^2}\cos^2\theta$$

$$\mathbf{B} = \frac{2\pi^2 r^2}{\lambda^2}\sin^2\theta$$

$$\mathbf{C} = 0.$$

Substituting the values $\mathbf{A}$ and $\mathbf{B}$ in Eqn. 14 gives the corresponding closed form equation of the CRB for the planar circular trajectory (Derivation in Appendix A (II)).

(c) $r \to \infty$ [Planar linear trajectory]. For simplicity, we consider a line segment of length $2\pi r$ at angle (a, b). This is parameterized in spherical coordinates as follows (dropping t and subscript i for brevity):

$$\xi_u = a, \quad \varphi_u = b, \quad \rho_u = r\tau$$

Thus, our CRB terms are:

$$\mathbf{A} = \sum_{u=1}^{M}\frac{4\pi^2(r(u-1)\Delta)^2}{\lambda^2}$$
$$(\cos\theta\sin(r(u-1)\Delta)\cos(\phi - b) - \cos(a)\sin\theta)^2$$

$$\mathbf{B} = \sum_{u=1}^{M}\frac{4\pi^2(r(u-1)\Delta)^2}{\lambda^2}(\sin\theta\sin(a)\sin(\phi - b))^2$$

$$\mathbf{C} = \sum_{u=1}^{M}\frac{4\pi^2(r(u-1)\Delta)^2}{\lambda^2}$$
$$* (\cos\theta\sin(a)\cos(\phi - b) - \cos(a)\sin\theta)$$
$$* (\sin\theta\sin(a)\sin(\phi - b))$$

We do not show a closed form for the CRB for a line, as the 'u' term is not inside a trigonometric function and the CRB quickly inflates to infinity, except in certain directions where the trigonometric terms go to zero. That is, depending on the direction, linear trajectories are largely uninformative.

7.1.2 Observations: We note a few observations from our analysis by comparing the 2D circle to the 3D helix. The off-diagonal terms of our CRB matrix (Eqn. 5), are always zero for the case of 2D circle. This results in a
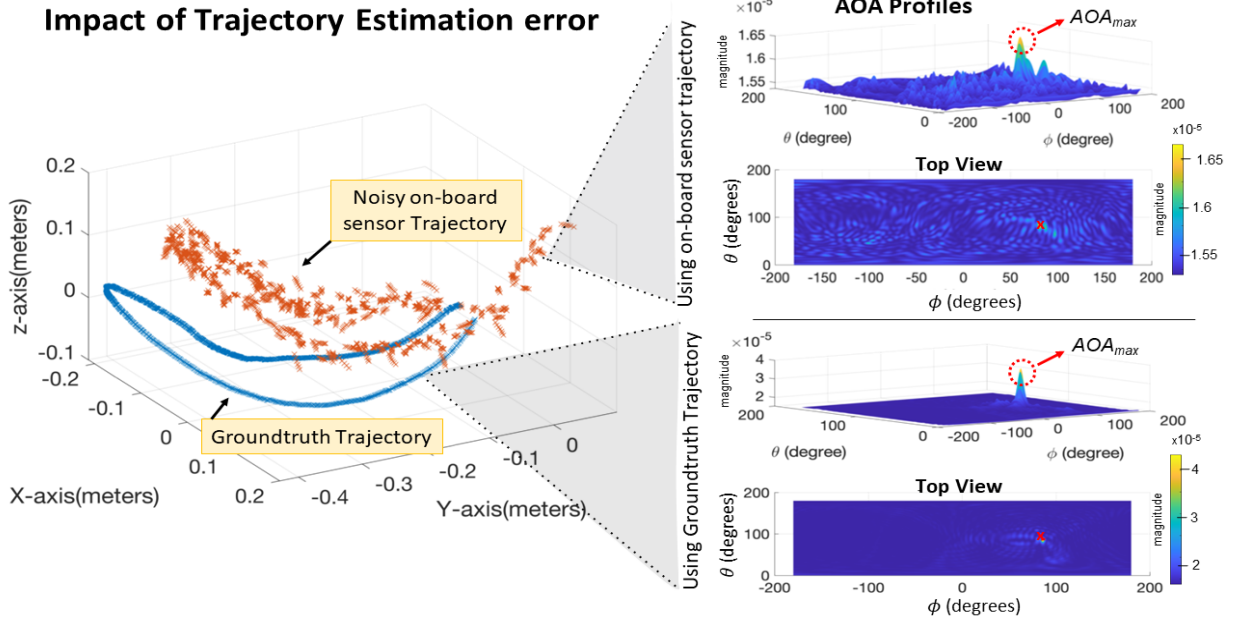
Figure 11. *Shows the AOA profile $F_{ij}(\phi, \theta)$ using groundtruth and Intel Realsense T265 tracking camera trajectories obtained from hardware experiment. The peak AOA_{max} in the in $F_{ij}(\phi, \theta)$ corresponds to the strongest signal direction of transmitting robot. Error in the estimated trajectory increases the error in AOA_{max} estimation and results in a more noisy profile (top right). The groundtruth AOA angles are marked by red 'x' in the Top View of the $F_{ij}(\phi, \theta)$. We see that there is a clear attenuation of the AOA_{max} and a slight shift for the tracking camera trajectory compared to the peak obtained from groundtruth trajectory. Aggregate results comparing the groundtruth and tracking camera trajectories are shown in Fig. 21.*

decoupling of the CRB in the θ and ϕ directions. When the transmitting robot is located in the x-y plane i.e $\theta = \frac{\pi}{2}$, CRB_θ for the planar circular case tends to infinity (as the **A** term becomes 0) while it remains finite for the 3D geometry case, thus the variance for the 2D trajectory increases (i.e. its informativeness decreases) as compared with the 3D trajectory case for some relative angles between receiving and transmitting robots. The high variance in performance of AOA estimation for the planar 2D case is sometimes referred to as the ambiguity problem of planar circular trajectory along elevation direction (Vu et al., 2011). Note that this is not the case for 3D trajectories which do not experience a variance increasing arbitrarily high for any transmitting robot locations relative to receiving robot. This theoretical finding is supported by hardware experiments (Fig. 16) which shows that 2D curved trajectories are more ambiguous along θ. Further, we note the **B** term for a helix is always higher than for the planar circle by a factor of at least π, which results in a tighter bound for ϕ for a helical trajectory.

In addition to observations from our derivation, we also note some observations on the CRB from simulated trajectories of receiving robot. This data was collected by simulating trajectories of a fixed length in each of the aforementioned shapes: a circle, a line, and a spherical helix. Then, the Cramer-Rao Bound (cf. Eqn. 14) was calculated for a simulated transmitting robot in each angular position between 1 and 360 degrees in each the ϕ and θ directions, for a total of 129600 possible transmitting robot locations. The CDF of the CRBs across all positions are shown in Fig. (10). We see the tightest bound on the helix, followed by the circle and then the line, thus ranking these common trajectories in terms of informativeness.

7.2 Characterizing the impact of trajectory estimation error on Angle-of-Arrival estimation

As an implementation of SAR requires knowledge of local robot displacements (see Section 5), one must rely on trajectory estimation techniques for robots operating in a field. Most often, robot displacements can be estimated using onboard sensors such as inertial measurement units (IMU), cameras, or LiDAR for trajectory estimation. However the error in a local trajectory $\hat{\chi}_i(\mathbf{t})$ due to different estimation approaches translates into error in steering vector (incorrect antenna positions) when used for SAR. Thus, it is necessary to analyze our system's performance under cases where the measured displacement is different from groundtruth displacement.

Since, our method requires only *local* displacement (sub-trajectory) information, it is not impacted by large accumulations of errors. Specifically, for any given AOA profile calculation only the sub-trajectory of positions as indicated by $\hat{p}(t)$ from $t = [t_k, \ldots, t_l]$ are used to emulate a virtual antenna array (See Fig. 5); This means that at any specific instance of 3D SAR, robot positions at timesteps not between $t_k, \ldots, t_l$ are irrelevant for AOA estimation. Thus, our development here focuses on impact of $\hat{\chi}_i(\mathbf{t})$ and the residual errors (Defn. 4) accumulated over $\hat{\chi}_i(\mathbf{t})$, on *AOA*. Comparing the results for groundtruth and Intel Realsense T265 tracking camera trajectories from hardware experiments (Fig. 11) we see that higher error in the latter impacts the estimated AOA profile. Our goal in this section is to mathematically model and analyze this impact as a function of trajectory estimation error.

We use the angular drift metric from Defn. (2) to quantify the residual error in trajectory estimation for our theoretical
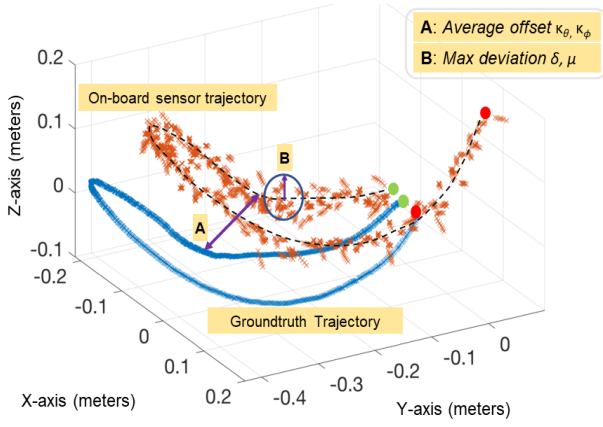
Figure 12. *Hardware experiment showing the drift in Intel Realsense T265 tracking camera trajectory compared to groundtruth trajectory.The end positions points (red) are much further away from each other than the start points (green) indicating drift accumulation.*

analysis. We assume that the errors for position $(x_i(t), y_i(t), z_i(t))$ in Cartesian coordinates are translated to errors in $\varphi_i(t)$ and $\xi_i(t)$ only in the corresponding spherical coordinates. We introduce two lemmas to show the impact of constant and varying angular drift on AOA estimation. To simplify our analysis, we use ideal circular arc trajectories in 3D and show that results for arbitrary 3D trajectories from hardware experiments closely follow our theoretical findings.

7.2.1 Constant offset: We first analyze the case of a constant offset; for example, as would occur in the case of a bias or drift in the trajectory estimation. We use a circular 3D trajectory of radius R to simplify the analysis.

Lemma 2. *If the measured trajectory in spherical coordinates is incorrect by a constant azimuth offset κ_ϕ and a constant elevation offset κ_θ, the observed AOA peak will occur at a shifted angle of $\phi - \kappa_\phi$, $\theta - \kappa_\theta$.*

Proof: Assume that the transmitting robot j at a point (D, ϕ, θ) is very far from the receiving robot i's trajectory, which is the arc of a circle of radius R. The distance from robot j to the bottom of the trajectory arc is given by $D - R\cos\phi\cos\theta$. By rotating our coordinate system, we get $D - R\cos(\phi - \varphi(t_u))\cos(\theta - \xi(t_u))$ as the distance from robot j to an arbitrary point on our arc, given robot j's (ϕ, θ) and virtual antenna element location $(\varphi(t_u), \xi(t_u))$ on robot i's trajectory. Thus, applying the general model of the wireless channel (Eqn. 1) for a circular trajectory based on distance D and radius R of the receiving robot trajectory, our forward-reverse channel product at a given $(\varphi(t_u), \xi(t_u))$ is the following (dropping notation t in RHS of the equation for brevity):

$$h_{ij}(t_u) = \frac{1}{D^2} e^{\frac{-4\pi\sqrt{-1}\ D}{\lambda}} * e^{\frac{-4\pi\sqrt{-1}\ \rho\ cos(\phi-\varphi_u)cos(\theta-\xi_u)}{\lambda}}$$
(15)

Due to some constant drift $\kappa_\phi, \kappa_\theta$, however, we instead measure a peak at some angle $\hat{\phi}$ rather than at ϕ, and some angle angle $\hat{\theta}$ rather than at θ, defined from the AOA profile

(cf. Eqn. (12)) as follows:

$$F_{ij}(\phi,\theta) = \frac{1}{D^2} \sum_{u=1}^{M} e^{\frac{-4\pi\sqrt{-1}\ D}{\lambda}} *$$

$$e^{\frac{-4\pi\sqrt{-1}\ \rho[cos(\phi-\varphi_u)cos(\theta-\xi_u)-cos(\hat{\phi}-\varphi_u+\kappa_\phi)cos(\hat{\theta}-\xi_u+\kappa_\theta)]}{\lambda}}$$
(16)

This takes the form of the well-known Bessel function, which is maximized at $\hat{\phi} = \phi - \kappa_\phi$ and $\hat{\theta} = \theta - \kappa_\theta$ (Mathews and Zoltowski, 2020).

7.2.2 Varying offset: Beyond constant offsets such as drift or bias, other errors that may complicate our analysis include the vibrations of drones and time-varying drifts in trajectory across narrow data-capture windows. Our following analysis considers the effect of this varying offset (Fig. 12).

Lemma 3. *For a measured trajectory incorrect by some average offset κ_ϕ with a max deviation of δ around κ_ϕ in the azimuth direction, and some average offset κ_θ with a max deviation of μ around κ_θ, there will exist a peak located at angle $(\phi - \kappa_\phi, \theta - \kappa_\theta)$, in line-of-sight conditions. This peak will attenuated by a factor no more than $cos(\frac{\delta+\mu}{2})$, relative to the peak in absence of trajectory offsets.*

Proof: We consider the *phase* component $\angle F(\phi, \theta)$ of Equation 16 (in the exponent) from the previous lemma, substitute a= $\phi - \varphi_u$ and b= $\theta - \xi_u$ and modify it for a varying κ_ϕ and κ_θ, indicated by subtracting deviations from the mean for each position, δ_u, μ_u:

$$\angle F(\phi,\theta) = \frac{-4\rho\pi\sqrt{-1}}{\lambda}[cos(a)cos(b) - cos(a-\delta_u)cos(b-\mu_u)]$$
(17)

Assuming δ_u and μ_u are relatively small, we can simplify our equation using trigonometric identities to the following:

$$\angle F(\phi,\theta) = \frac{-4\rho\pi\sqrt{-1}}{\lambda}[\delta_u\ sin(a)cos(b) + \mu_u\ sin(b)cos(a)]$$
(18)

Consider the worst-case scenario, where $\delta = \delta_{max}$ and $\mu = \mu_{max}$, and $\delta = -\delta_{max}$ and $\mu = -\mu_{max}$, alternately. For brevity, we represent the quantity $\frac{1}{D^2} e^{\frac{-4D\pi\sqrt{-1}}{\lambda}}$ with α, and group these alternate phases together (thus changing the bounds of our summation). We can rewrite our profile as follows:

$$F_{ij}(\phi,\theta) \geq \alpha \sum_{u=1}^{M/2} e^{\frac{\sqrt{-1}\ (\delta_{max}+\mu_{max})}{2}} + e^{\frac{-\sqrt{-1}\ (\delta_{max}-\mu_{max})}{2}}$$

$$\text{i.e. } F_{ij}(\phi,\theta) \geq \alpha M cos\frac{\delta_{max}+\mu_{max}}{2}$$
(19)

Thus, our peak at $\phi - \kappa_\phi$, $\theta - \kappa_\theta$ from Lemma 1 is attenuated by a factor that is at most $cos\frac{\delta_{max}+\mu_{max}}{2}$ vs. the peak in the absence of drift.

Our hardware experiment results bolster these theoretical findings. A representative trace is shown in Fig. 11, which provides comparison between two wireless signal profiles using motion capture versus a tracking camera. The side view for the profiles indicates an attenuation of the maximum

AOA peak as expected from the analysis of this section. From a top view the predicted peak shift can also be seen for the trajectory estimation case ("using Noisy Estimated Trajectory" case) versus the case where motion capture is used to provide the trajectory estimate.

Section 8.4 demonstrates aggregate results showing the impact of trajectory estimation error on AOA error on average, where robot trajectories are estimated using an Intel RealSense T265 tracking camera. It also includes results for a simulation study demonstrating the relationship between increasing trajectory estimation error and AOA estimation error (see Fig. 19).

8 Results

In this section we present the results of extensive simulation and hardware experiment studies that demonstrate agreement of practical implementations with the development and analysis sections of the paper. In particular we study 1) the feasibility of attaining accurate AOA profiles $F_{ij}(\phi, \theta)$ using relative trajectory of a receiving robot in the moving ends case where both transmitting and receiving robots are simultaneously mobile, 2) the informativeness of different trajectory geometries in 2D and 3D, and 3) the impact of trajectory estimation errors on attainable AOA_{max} accuracy. We find that:

- Our developed framework from Section 6 solves the *moving ends* problem where $F_{ij}(\phi, \theta)$ is attainable even when both the transmitting and receiving robots are simultaneously moving. Furthermore in this case, *relative* trajectories being more informative lead to higher accuracy of $F_{ij}(\phi, \theta)$.
- Arbitrary 3D trajectories generate highly accurate $F_{ij}(\phi, \theta)$ (less than 10 deg error in AOA_{max} for 95% of trials). In contrast, planar 2D curved and linear trajectories only 50% and 7% of trials show error below 10 deg respectively.
- For robot trajectory estimates with an average of 5% estimation error obtained using an on-board Intel RealSense T265 Tracking camera (0.06m error in position over 1.2m long trajectories), attainable AOA_{max} estimation accuracy was shown to be within 10.03 degrees in azimuth and 2.23 degrees in elevation on average.

We subsequently describe our experimental setup in section 8.1. The results for moving ends experiments are detailed in section 8.2. Section 8.3 and 8.4 show the results for trajectory informativeness and the impact of trajectory estimation respectively.

8.1 Experimental setup

Testbed and hardware setup: We use an off-the-shelf *Turtlebot3 Waffle* for our ground robot and an *NXP KIT-HGDRONEK66* drone for our aerial robot (Fig. 4). Each robot is mounted with a lightweight 2 DBi omnidirectional WiFi antenna, *UP Squared* on-board computer which uses an Intel 5300 WiFi module and an out-of-the-box *Intel Realsense T265* tracking camera which gives local pose estimates at 200 Hz. We evaluate our system in a 10,000 square feet, 23-foot-tall indoor environment.
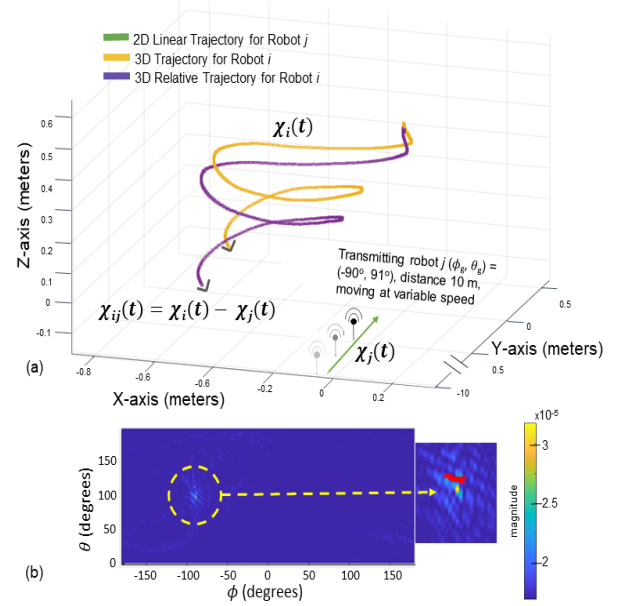

Figure 13. *(a) Hardware experiment showing the 3D trajectory for UAV* $\chi_i(t)$ *and the corresponding relative trajectory* $\chi_{ij}(t)$ *due to motion of transmitting robot* j *with trajectory* $\chi_j(t)$*. Our approach for moving ends gives similar profile results for 3D trajectories as seen in Fig. 6. (b) AOA profile showing true Angle-Of-Arrival* $(\phi_g, \theta_g) = (90°, 91°)$*, denoted by red 'x' in the profiles.*

Using 105 cameras, the *Optitrack* motion capture system deployed in the testbed provides groundtruth measurements for robot trajectories and relative AOA between them. Using groundtruth trajectories, we first obtain a benchmark performance for our system. A second set of experiments using Intel Realsense T265 tracking camera trajectories is conducted to understand how $F_{ij}(\phi, \theta)$ and AOA_{max} are impacted when using position information from VIO systems since they have become ubiquitous to mobile robot platforms in recent years.

For experiments with groundtruth trajectories the center of the rigid body model generated by motion capture system is aligned with the physical placement of WiFi antenna on the robots' chassis. For experiments with tracking camera trajectories, the antenna and T265 camera are aligned on the robots' chassis and their offset, if any, is accounted for. The robots use minimal communication (broadcasting ping packets) over the center frequency channel of 802.11 5GHz band. The total data transmission overhead for our system amounts to a maximum of 15 kB in 3 seconds when a receiving robot performs 3D SAR. Note that the frequency of such transmission would highly depend on the application. In our dynamic rendezvous hardware application (Sec. 9), as the receiving robot continuously requires AOA_{max} for navigation, this leads to an average 5kB/s transmission overhead. This includes phase information collected from transmitted signals between robots and local position estimates from neighboring robots (in their own coordinate frame).

Pose estimates from the tracking camera and channel information from transmitted signals are collected using each robots' on-board computer. The current nature of our code-base requires processing the data on an off-board computer but the computation requirements for our system
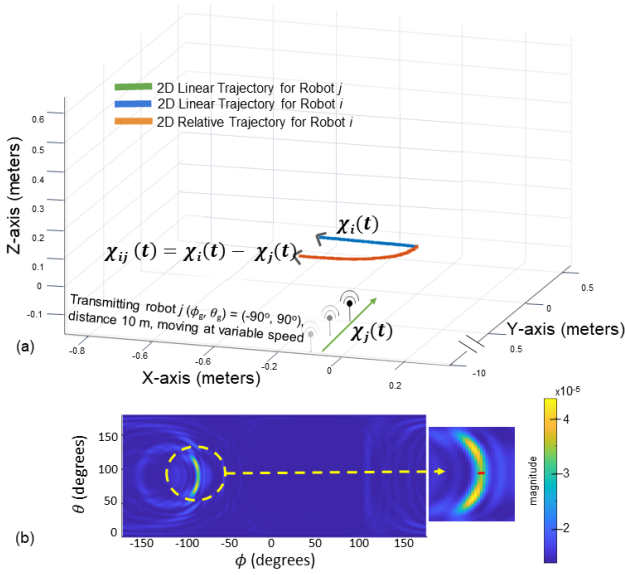
Figure 14. *(a) Hardware experiment showing linear 2D trajectory $\chi_i(t)$ for signal receiving robot i and the corresponding curved relative trajectory $\chi_{ij}(t)$ due to motion of transmitting robot j with trajectory $\chi_j(t)$. Using the relative trajectory, our approach for moving ends (Sec. 6) gives similar profile results for 2D curved trajectories (Fig. 6) with ambiguity only along elevation angle. (b) AOA profile showing $(\hat{\phi}, \hat{\theta}) = (-90°, 73°)$ while true AOA $(\phi_g, \theta_g) = (-90°, 90°)$, denoted by red 'x' in the profiles. Relative trajectory $\chi_{ij}(t)$ (curved 2D) thus has a more informative geometry than actual trajectory $\chi_i(t)$ (linear 2D).*

are satisfied by on-board computer as well. All processing is done in real time. We use both Bartlett and MUSIC estimators (Krim and Viberg, 1996) for generating $F_{ij}(\phi, \theta)$ and our results indicate which estimator was used. We note that our theoretical analysis in Section 7.2 uses a Bartlett formulation and thus all trajectory error experiments (Sec. 8.4) were conducted using the Bartlett estimator.

Software setup: We use Ubuntu 16.04 with kernel 4.15, as the OS for the on-board computer. It runs the following: Drone control that uses ROS and MAVROS, pose estimation from realsense libraries for the tracking camera[1] and a modified iwlwifi driver with 802.11 CSI toolbox (Halperin et al., 2011) that collects wireless channel state information (CSI), which is used to calculate signal phase. The AOA profile is calculated in an off-board fashion using a laptop that runs a Matlab framework. As per our assumption, global clock synchronization among the robots is achieved by running ntpd at the start an experiment.

8.2 Moving ends

Our SAR development allows for generating AOA profile $F_{ij}(\phi, \theta)$ using arbitrary 3D trajectories for a static transmitting robot (Sec. 5). Extending that formulation to the *moving ends problem*, in this section we demonstrate the accuracy of the resulting $F_{ij}(\phi, \theta)$ obtained using relative trajectory $\chi_{ij}(t)$ with mobile receiving and transmitting robots i and j. Relative trajectory can be obtained using different onboard sensors, however for proof-of-concept purposes of our developed framework, we provide position estimates of local robot trajectories using an external motion capture system. The following scenarios are evaluated:

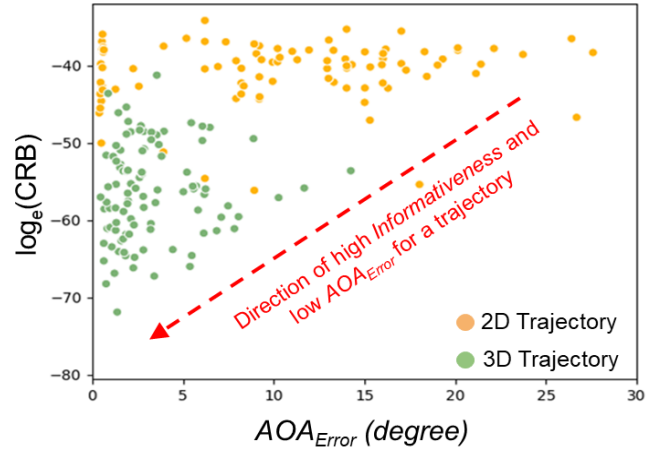1. Robot i performs a helix motion at 0.5 m/s (Fig. 13)

Figure 15. *Aggregate results comparing 2D and 3D trajectories obtained from hardware experiments in terms of AOA_{Error} (Eqn. 7) and Cramer-Rao bound. A low of value of CRB indicates that the trajectory has high informativeness. From the distribution of CRB and AOA error for 2D and 3D trajectories, 3D trajectories have a lower AOA_{Error} on account of being more informative than 2D trajectories.*

2. Robot i performs a linear motion at 0.1 m/s (Fig. 14)

and the transmitting robot j moves along a linear trajectory with varying speed (max speed of 0.1m/s), and is at a distance of 10 meters from robot i. Results for the 3D scenario using a sample trajectory from hardware experiments are shown in Fig. 13. We see that $F_{ij}(\phi, \theta)$ obtained using relative trajectories for a moving transmitting robot show similar behavior when compared to those obtained for a static transmitting robot (Fig. 6).

We make interesting observations with respect to the use of relative trajectories. For example, when the transmitting and receiving robots are moving linearly along different directions and with different speeds, the relative trajectory obtained has a curved geometry which eliminates ambiguities along ϕ (Fig. 14). Thus, we postulate that depending on the direction and variation in speed of the moving robots, more informative and less ambiguous trajectories can be naturally obtained. Further investigation of this observation, namely, exploiting relative trajectories for obtaining higher informativeness from 2D trajectories, is an interesting avenue for further research. Results pertaining the informativeness of different trajectory geometries are discussed in the following section.

8.3 Informativeness of 2D and 3D trajectories

In this set of experiments our objective is to study the impact of trajectory geometry on AOA_{max} estimation. In order to isolate the effect of trajectory geometry from other factors such as position estimation errors, the results of this section use groundtruth robot trajectories obtained from motion capture (the effect of position estimation errors is studied subsequently in Section 8.4). For a single experiment, relative AOA_{max} is computed between a static ground robot (signal transmitting) and a signal receiving robot moving along a trajectory of one of the following three types - 2D linear trajectory, 2D curved trajectory and 3D arbitrary trajectory (See Fig. 16). We call such an experiment a *trial* and conduct a total of 101 *trials* for each type of trajectory.
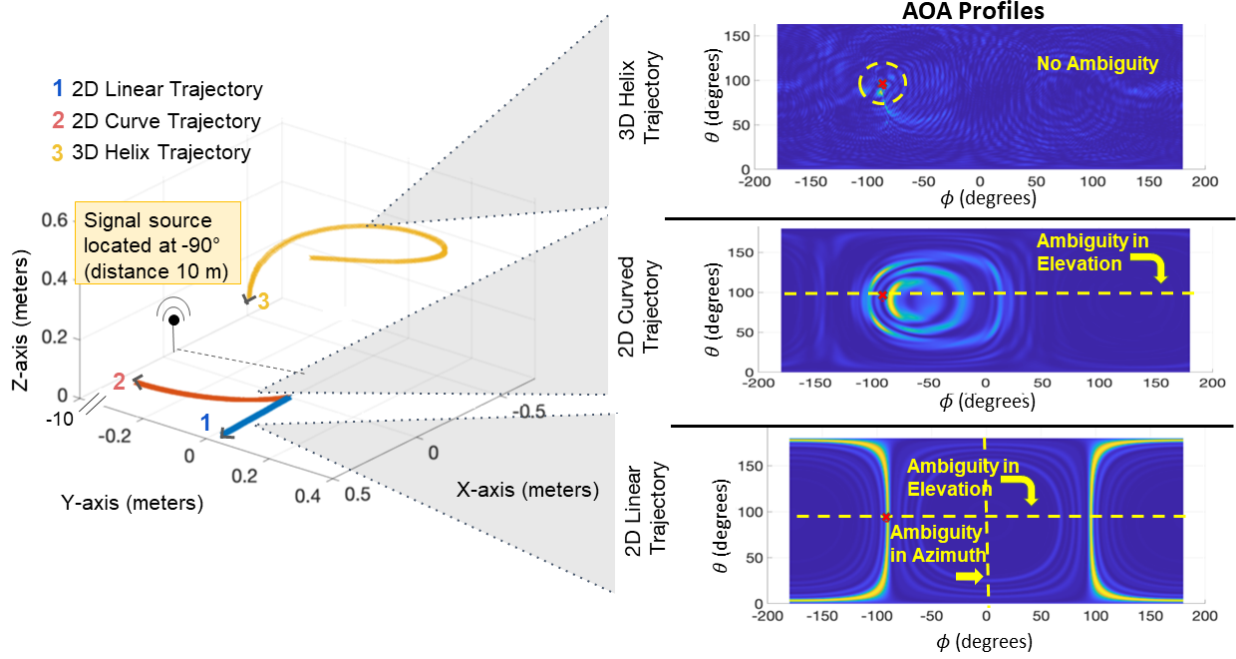
Figure 16. *Shows different trajectories (left) obtained from hardware experiments and ambiguities in the AOA profile $F_{ij}(\phi, \theta)$ (right). True AOA ($\phi_g, \theta_g) = (-90°, 91°)$ to the WiFi signal source (i.e transmitting robot) is denoted by red 'x' in the profiles. 3D trajectories have higher informativeness and have no ambiguities in the AOA profile (top right).*
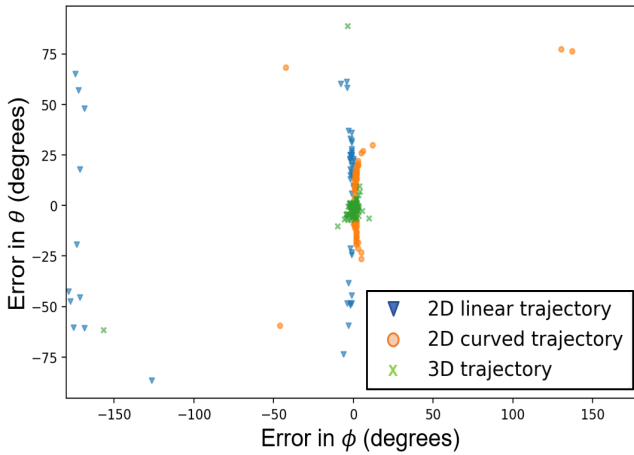

Figure 17. *Aggregate benchmark results using groundtruth trajectories that show AOA error in azimuth angle ϕ and elevation angle θ (Defn. 3). The profiles are generated for 101 hardware experiment trials each for the three trajectory types (2D linear, 2D curved and arbitrary 3D). 3D trajectories (green) have higher AOA accuracy in both azimuth (ϕ) and elevation (θ) directions as compared to 2D trajectories, which show high error in θ (curved trajectory). Moreover 2D linear trajectories have additional errors in ϕ. Thus, the aggregate results align with those shown in Fig. 16 for individual samples of each trajectory type.*

For this set of experiments the robots are separated by a distance of 10m and are in line-of-sight of each other to exclude other impacting factors. The application of our system to non-line-of-sight scenarios is studied subsequently in Section 9.

We note that informativeness is defined in both the azimuth and elevation directions and while 3D trajectories demonstrate high informativeness in both directions, 2D curved trajectories perform better in azimuth (ϕ) and worse in elevation (θ). Fig. (15) demonstrates that the *informativeness* calculated for each trajectory (inverse of

the CRB) successfully captures this improved performance in AOA_{Error} for 3D versus 2D trajectories. This provides empirical evidence of the analysis derived in Section 7.1 which predicts higher informativeness (smaller attainable CRB) for 3D trajectories. Fig. (18) shows the aggregate performance over 101 trials of each of three different trajectory types: 2D linear, 2D curved, and 3D. Overall AOA_{Error} (Fig. 18 (a)) is significantly lower for 3D trajectories as compared to its 2D counterparts. Specifically, 3D trajectories demonstrate less than 10° AOA_{Error} for 95% of the total trajectory samples within the same type, where as only 50% of 2D curved trajectories and 7% of 2D linear trajectories show similar accuracy. This trend is again shown empirically in our application scenario results in Section 9.

Hardware results also reveal important intuition behind the informativeness of different trajectory geometries. Fig. (16) demonstrates a typical trial for each of the three trajectory types studied in this paper. Here it is shown that for trajectory types of lower informativeness such as the linear 2D trajectory, ambiguities are observed in $F_{ij}(\phi, \theta)$ for relative direction $(\hat{\phi}, \hat{\theta})$ of the transmitting robot. This is due to the inability of the linear antenna array geometry traced by receiving robot to uniquely distinguish a transmitting robot's location for certain direction tuples (ϕ, θ) using phase differences. This problem is greatly alleviated by using trajectories with high levels of informativeness (3D trajectories).

In conclusion, our results clearly indicate that 3D trajectories have the highest informativeness amongst all trajectory types studied, resulting in more accurate estimation of AOA_{max} in both azimuth and elevation, as predicted by the analysis from Section 7.
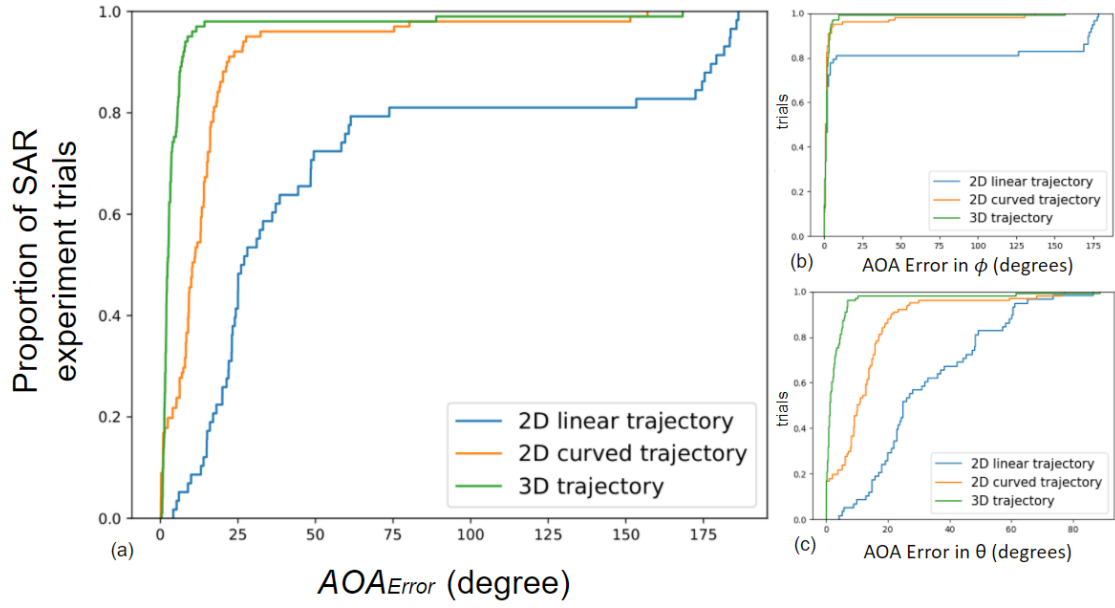
Figure 18. *Benchmark results obtained using groundtruth trajectories for a receiving robot in hardware experiments. The transmitting robot is at a distance of 10m. (a) CDF plot for AOA_{Error} error for 101 trials of each trajectory type (linear, curved and arbitrary 3D). 3D trajectories have the lowest AOA_{Error} (Defn. 3) which is less than $10°$ for 95% of trials. For planar 2D curved and linear trajectories only 50% and 7% of trials show error below $10°$ respectively. (b) and (c) show the individual CDF plots for AOA error in ϕ and θ respectively. 2D linear trajectories have the highest error overall. We note that even groundtruth trajectories incur AOA error due to factors mentioned in Sec. 4.3.*
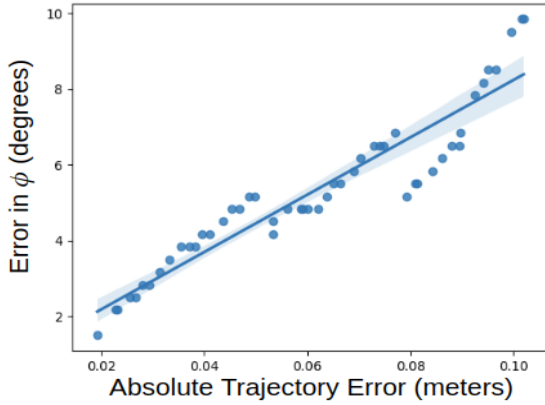

Figure 19. *Simulation Results showing Angle-Of-Arrival estimation error vs Absolute Trajectory error in translation (ATE_{trans}: Eqn. 6). Trajectory error is added using simulated noise to a groundtruth trajectory of receiving robot obtained in hardware experiments. The range of ATE_{trans} on X-axis reflects the observed error in Intel Realsense T265 tracking camera trajectories (Fig. 20).*

Figure 20. *Absolute Trajectory Error (ATE_{trans}: Eqn. 7) observed for Intel Realsense T265 tracking camera trajectories obtained from our hardware experiments.*

8.4 Effect of trajectory estimation error on AOA

As computing AOA profiles $F_{ij}(\phi, \theta)$ requires knowing a robot's local displacement and most robots in the field rely on onboard sensors to estimate their position, in this section we experimentally study the impact of trajectory estimation on $F_{ij}(\phi, \theta)$. We do so by measuring the AOA_{max} (maximum magnitude path in $F_{ij}(\phi, \theta)$) accuracy in presence of trajectory estimation errors. Our empirical analysis includes both a simulation and a hardware component where the simulation provides a controlled study in which noise can be added systematically to reveal error trends, and the hardware component provides aggregate results showing the impact of trajectory estimation error on AOA_{max}
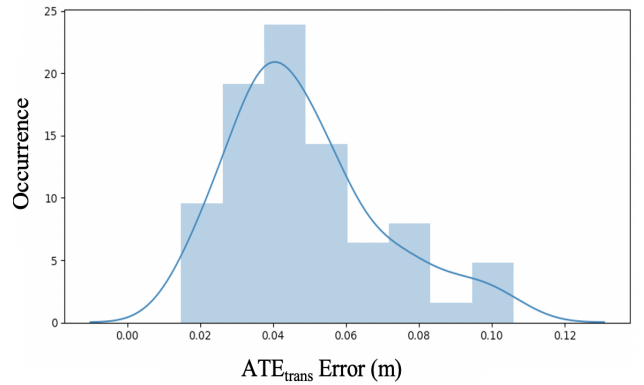
accuracy in an actual all on-board sensing robot system. For the hardware experiments we use trajectory estimates provided "out-of-the-box" from the tracking camera. No additional optimization techniques were used to improve trajectory estimation though we do note that it is possible to obtain better trajectory estimation using state-of-the-art methods and sensors (See Sec. 2). The AOA_{max} estimates obtained are compared against benchmark results from using groundtruth trajectories (obtained from motion capture system).

8.4.1 Simulation study: Our simulation study emulates accumulating error in trajectory estimates in the following way: we generate multiple noisy trajectories $\hat{\chi}_i(t)$ by adding accumulating Gaussian noise to a sample 3D groundtruth trajectory $\chi_i(t)$ of the receiving robot i. $F_{ij}(\phi, \theta)$ is then generated for these $\hat{\chi}_i(t)$ to obtain an AOA_{max} estimate
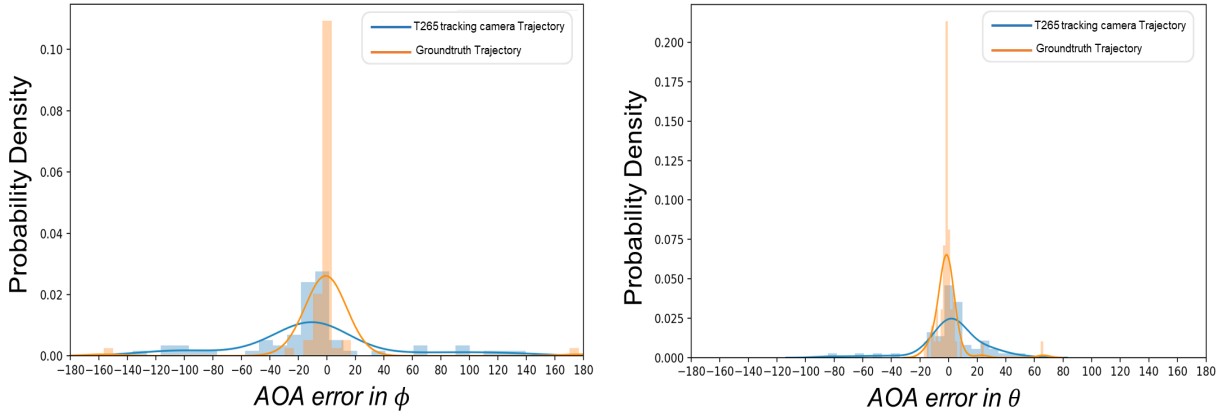
Figure 21. _Aggregate results of AOA estimation for 59 hardware experiments. Each experiment records the Intel Realsense T265 tracking camera trajectory and groundtruth for the receiving robot along with their respective $F_{ij}(\phi, \theta)$. Groundtruth AOA (ϕ_g, θ_g) = $(0°, 91°)$. Sub-plot on the left shows error in ϕ with mean = -0.63 degrees for groundtruth trajectory and -10.03 degrees for tracking camera trajectory. Sub-plot on the right shows error in θ with mean = -0.69 degrees for groundtruth trajectory and 2.23 degrees for tracking camera trajectory. Thus, with high error in estimated trajectory, the corresponding AOA accuracy is low, compared to that obtained from groundtruth trajectory._

$(\hat{\phi}, \hat{\theta})$ which is then compared with the true simulated AOA direction (ϕ_g, θ_g) to compute AOA error (cf. Defn. 3).

In order to generate an $F_{ij}(\phi, \theta)$ (cf. Eqn. (12)) using simulated noisy trajectories as described above, we must also simulate the wireless channel $\mathbf{h_{ij}(t)}$ from the static transmitting robot j, obtained over these trajectories i.e over $\boldsymbol{\chi_i(t)}$. To simulate the wireless channel, we fix the virtual location $\hat{p}_j(t_k)$ of static j at 10m from position $p_i(t_k)$ in $\boldsymbol{\chi_i(t)}$. For any position $p_i(t)$, $t \in [t_k, \ldots, t_l]$ where k=0, l=500 and $d_{ij}(t)$ is the distance between $p_i(t)$ and $p_j(t_k)$, the channel measurements $h_{ij}(t)$ can thus be simulated from Eqn. 1 to obtain $\mathbf{h_{ij}(t)}$. As AOA_{max} captures relative angle information, we simulate noise in $\boldsymbol{\chi_i(t)}$ by applying increasing cumulative angular error in $\varphi_i(t)$ and $\xi_i(t)$ for each $p_i(t)$ (is represented in polar coordinates) in $\boldsymbol{\chi_i(t)}$. We assume that the errors for position $(x_i(t), y_i(t), z_i(t))$ in Cartesian coordinates are translated to errors in $\varphi_i(t)$ and $\xi_i(t)$ only in the corresponding Spherical coordinates.

$\boldsymbol{\hat{\chi}_i(t)}$ are simulated in such a way that their ATE_{trans} error (cf. Eqn. (6)) are representative of those characteristic from using on-board sensors. This is based on our observations of estimation error using tracking camera (see Fig. 20). In particular, to generate the first noisy trajectory, for each position $p_i(t)$ in $\boldsymbol{\chi_i(t)}$, we sample angular error (in degrees) from a Gaussian distribution. This is then repeated for all $\hat{p}_i(t)$, with the errors being cumulatively added for successive positions. The noise is simulated in a way that the accumulating error in the trajectory would reflect realistic ATE as we obtained in Fig. 20 from the tracking camera on the drone. This generates $\boldsymbol{\hat{\chi}_i(t)}$ from $\boldsymbol{\chi_i(t)}$ with an accumulating angular drift. The corresponding ATE_{trans} error for $\boldsymbol{\hat{\chi}_i(t)}$ then is obtained by converting the noisy trajectory positions $\hat{p}_i(t)$ from spherical coordinates to Cartesian coordinates and then using Eqn. 6. To generate additional noisy trajectories, we increase the sampled angular error for each successive simulated trajectory steadily so that the ATE_{trans} error ranges from 0.02m to 0.12m. A total of 50 noisy trajectories are generated.

Our empirical results support our analytical development from _Lemma_ 2 and 3 (Sec. 7.2). The corresponding

ATE_{trans} error generated for simulated trajectories also shows a increasing linear relationship with AOA error (Fig. 19). Thus we conclude that trajectories with ATE_{trans} in the range (0.02, 0.12) will demonstrate an AOA estimation error in the range (2,10) degrees in the absence of other factors that impact $F_{ij}(\phi, \theta)$.

_8.4.2_ **_Hardware experiments:_** For hardware experiments, we compare AOA_{max} estimation using pose estimates obtained from Intel Realsense T265 tracking camera against benchmark AOA_{max} estimates obtained from groundtruth robot trajectories. Both trajectory types are simultaneously collected for the receiving robot using the tracking camera (mounted on the aerial robot) and an external motion capture system. AOA_{max} estimates are calculated in realtime, while keeping the transmitting robot static (results involving a mobile transmitting robot are presented in Section 8.2 and Section 9). Average robot trajectory lengths are 1.2m per AOA profile generated. Fig. (21) shows a Kernel Density Estimation (KDE) distribution plot comparing AOA estimation error in ϕ and θ for 59 trajectories using position estimates obtained via tracking camera trajectories versus the benchmark (obtained using groundtruth trajectories). The error mean in azimuth angle ϕ and elevation angle θ is -0.63 degrees, -0.69 degrees respectively for groundtruth trajectories, and -10.03 degrees, 2.23 degrees respectively for tracking camera trajectories. Fig. 20 shows an mean error of 0.06m for tracking camera trajectories which were 1.2m long on average. Thus the results shown in Fig. 21 represent average AOA_{max} estimation error for trajectories with an average of 5.0% estimation error. We note that our benchmark results represent an empirical lower bound for AOA_{max} estimation error attainable using robot trajectory estimation techniques with improved position estimation accuracy in the presence of other factors (e.g. trajectory geometry) that impact $F_{ij}(\phi, \theta)$.

9 Application Study

Dynamic rendezvous between ground/air robots

In this section, we demonstrate the performance of our system for a complete experiment of multi-robot rendezvous
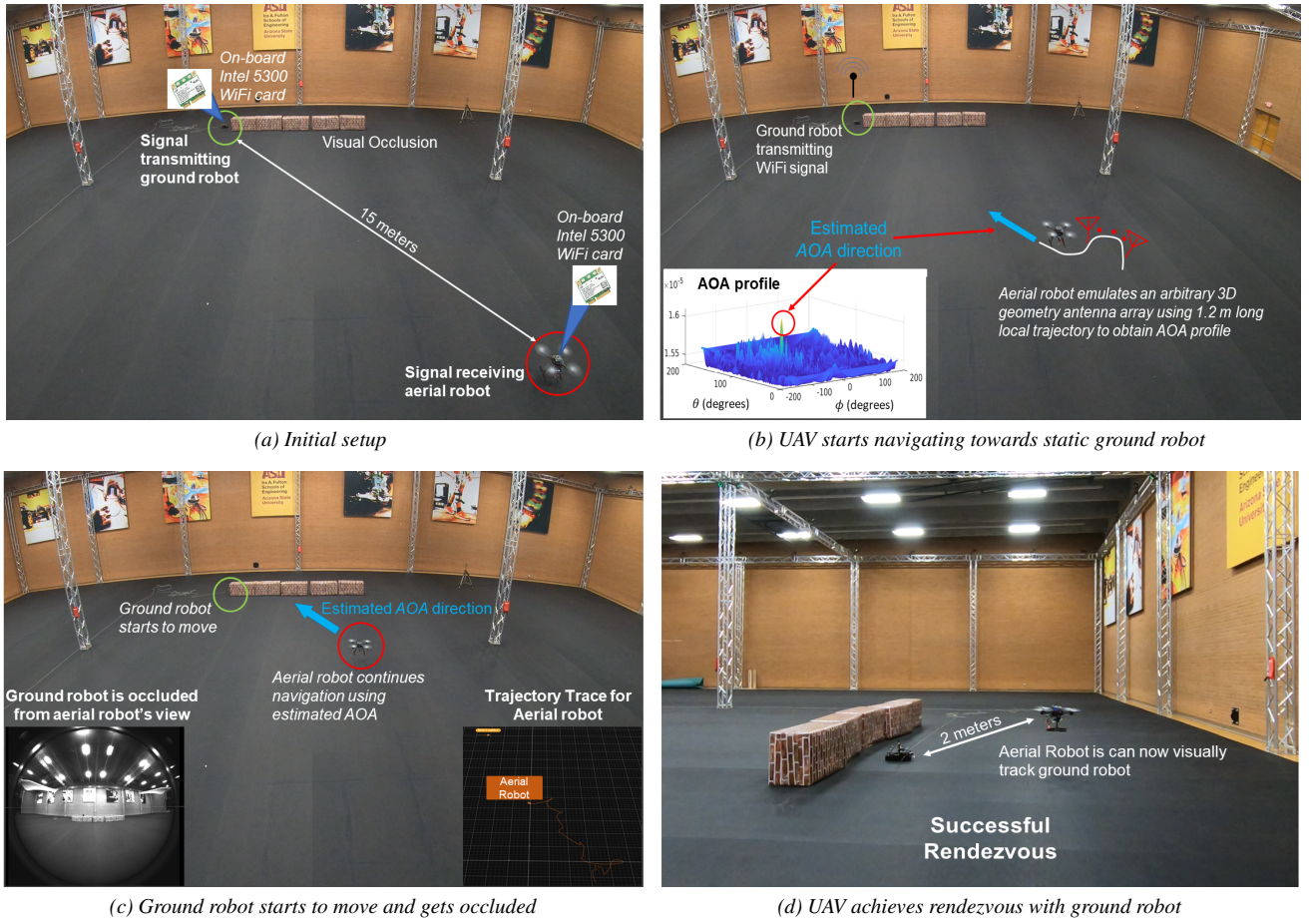
(a) Initial setup

(b) UAV starts navigating towards static ground robot

(c) Ground robot starts to move and gets occluded

(d) UAV achieves rendezvous with ground robot

Figure 22. *Shows different stages of dynamic rendezvous hardware experiment between signal transmitting ground robot and receiving UAV. Starting from top-left : a) The initial setup to test rendezvous of UAV with the ground robot in presence of occlusions. b) The UAV begins to navigate towards the stationary ground robot, leveraging relative AOA information obtained from continuously generating AOA profiles using our arbitrary 3D SAR system which leverages robot trajectory generated from its natural motion. c) The ground robot starts to move and gets occluded (UAV loses visual of the ground robot as seen in the fisheye view image). d) The UAV continues its navigation towards the ground robot despite of occlusion until it is within 2 meters proximity, at which point rendezvous is declared successful.*

task between a UAV (signal receiving) and a ground robot (signal transmitting), so as to evaluate the utility of our system for a multi-robot coordination application that involves a heterogeneous team of robots. Our evaluation is based on the following three criteria:

- *System performance in presence of occlusions*: We verify that the UAV can navigate towards the ground robot using relative AOA_{max} by continuously generating AOA profiles $F_{ij}(\phi, \theta)$ in realtime, even when the ground robot is occluded.
- *Performance of our system in the presence of moving ends*: We verify that the UAV continues it's navigation accurately even when the ground robot starts to move.
- *Impact of trajectory geometry*: Following the development in Sec. 7.1 we calculate the informativeness of trajectory geometry for each iteration of 3D SAR as the UAV navigates towards the ground robot.

Experimental setup: We consider an environment of size 300 square meters with one aerial and one ground robot separated by distance 15m and visual occlusions due to a wall of cardboard boxes. We note that these occlusions block visual line-of-sight but are penetrable by WiFi signals. Motion capture is used to provide displacement information

for the UAV (robot i). Information about the position of the ground robot (robot j) is not known to robot i who solely uses obtained AOA information from its measured $F_{ij}(\phi, \theta)$ to track robot j. True AOA is obtained between robot i and j using their respective positions from motion capture system.

At the start of the experiment, the robots are separated by a distance of 15m (Fig. 22 (a)). The UAV, after take-off, starts to successfully navigate towards the ground robot, that is initially static, using relative AOA_{max} obtained from wireless signal information and a simple waypoint motion controller (Fig. 22 (b)). The ground robot then starts to move and gets visually occluded by obstacles (Fig. 22 (c)), but the UAV continues to successfully navigate towards it. We consider the rendezvous successful when the UAV is within a 2m radius of the ground robot (Fig. 22 (d)).

We note that as stated in Sec. 4, the relative AOA_{max} to the robot j is calculated with respect to the initial position $p_i(t_k)$ of the robot i. Thus if the true AOA with respect to this initial position undergoes a substantial change over the data collection period, as could happen when agents are at short distances to one another or when robots are moving very fast relative to each other, then the AOA_{max} will be outdated. For our experiments UAV and ground robot are traveling at 0.5 m/s and 0.1 m/s respectively and once they are within 2 meters of each other we stop tracking using $F_{ij}(\phi, \theta)$ (at this
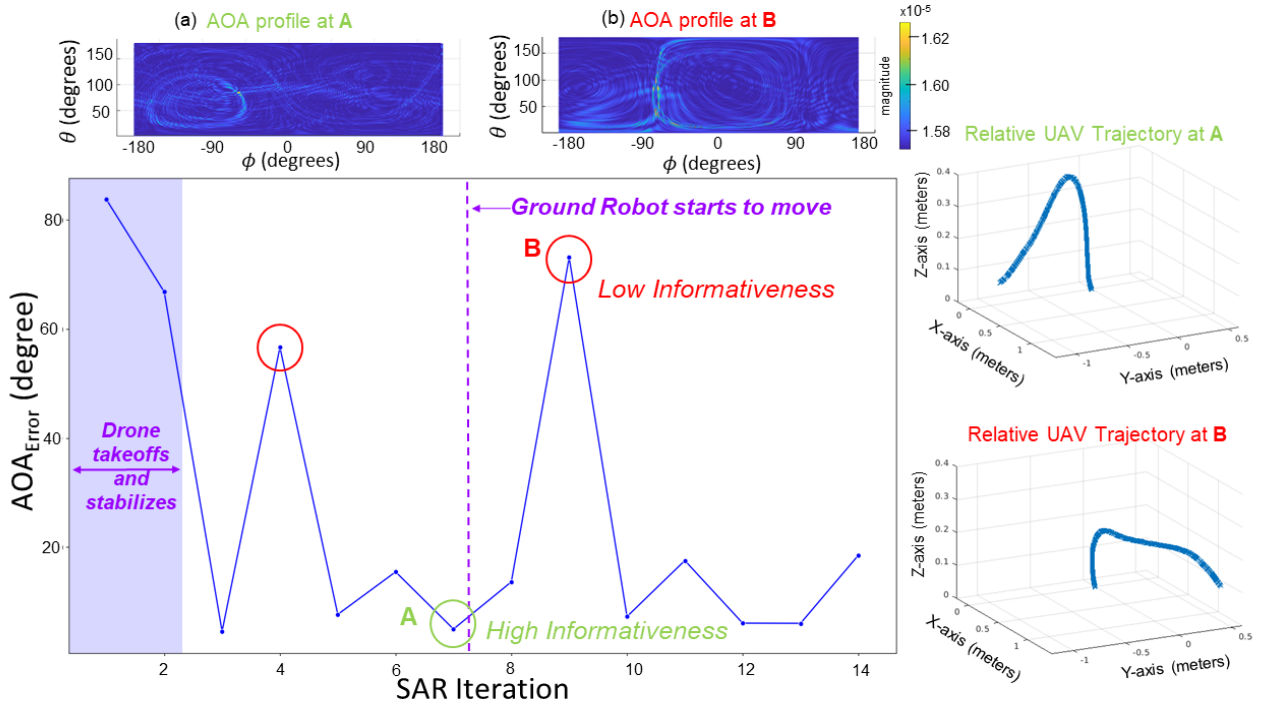
Figure 23. *Plot showing AOA_{Error} (Eqn.7) for signal receiving UAV during the dynamic rendezvous hardware experiment. Our approach takes into account the motion of transmitting robot (start indicated by vertical dotted line) while the UAV continues to navigate towards it. During each SAR iteration, the UAV travels a distance of 1.2 meter on average. AOA profiles and the UAV trajectory are shown for iteration 7 (point A) and iteration 9 (point B). High error at point B is due to low informativeness of the corresponding trajectory (show on the right) and an ambiguous $F_{ij}(\phi,\theta)$ (shown at the top). Similar behavior is observed for iteration 4. Conversely, the UAV trajectory at point A is highly informative and has almost no ambiguity leading to low AOA_{Error}. High AOA error for the first two iterations is due sudden jerk and high vibrations of the UAV chassis during take-off.*
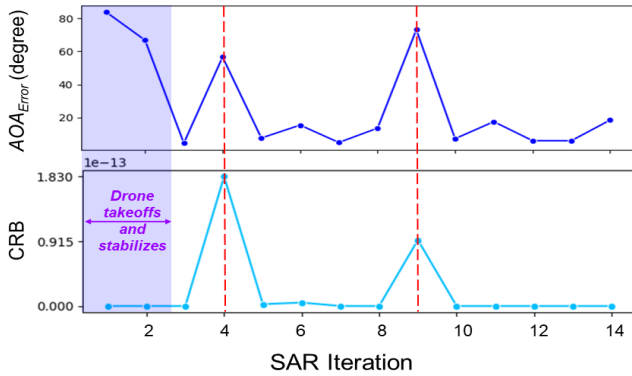

Figure 24. *Shows that CRB can be used to presage AOA accuracy that would result from low informative trajectories. The results are for trajectories obtained during the dynamic rendezvous hardware experiment. The high CRB values at timesteps 4 and 9 indicate lower trajectory informativeness and higher ambiguity in $F_{ij}(\phi,\theta)$ (see Fig. 23). Correspondingly we see high AOA_{Error} at those points. We note that despite the CRB being low for the first two iterations, the AOA_{Error} is high, generally due sudden jerk and high vibrations of the UAV chassis.*

point we assume that an on-board camera could be used to maintain tracking).

Evaluation: For evaluation of our system performance, we use AOA_{Error} (Eqn. 7) to measure the accuracy of our AOA_{max} estimation against groundtruth (from motion capture). Our evaluation focuses on the following: 1) evaluating AOA_{Error} over time, 2) evaluating AOA_{Error} for the moving ends case where both the transmitting and receiving robots are moving, and 3) experimental

characterization of the robot trajectory's *informativeness* versus AOA_{Error}.

We collect data over UAV trajectories which are 1.2 m long on average to measure a complete $F_{ij}(\phi,\theta)$. We refer to this as a *SAR iteration*. During a SAR iteration, the UAV uses its relative trajectory to generate $F_{ij}(\phi,\theta)$ and updates its waypoint to navigate towards the ground robot using estimated AOA_{max} from $F_{ij}(\phi,\theta)$. Fig. 23 shows the resulting accuracy of the AOA_{max} estimation for each iteration. When the UAV initially takes-off, we observe high AOA_{Error} (generally due sudden jerk and high vibrations of the chassis) before it stabilizes itself. Over the course of the experiment, the mean AOA_{Error} between robots is 10.17 degrees with the exception of two outlier points at iteration 4 and 9. Note that AOA_{Error} is not affected by the motion of the ground robot which begins at iteration 7. A closer look at iteration 9 and 4 reveals that the $F_{ij}(\phi,\theta)$ exhibits ambiguity peaks (ambiguous AOA directions) owing to sub-trajectories of low informativeness at these iterations (see Fig. 23 top (b)). Intuitively, this occurs when the trajectory of the UAV resembles a 2D trajectory with little displacement along the z-axis and is predicted by a high CRB (low informativeness) value at these points in the experiment (see Fig. 24). In contrast, all other iterations where the sub-trajectories of the UAV display high *informativeness* as characterized by the CRB, result in more accurate, less ambiguous, AOA peaks as shown in Fig. 23 top (a).

We make the following important observations:

- *Accurate AOA_{max} estimation with moving ends:* Despite the presence of a moving transmitting robot,

our 3D SAR system enables the signal receiving UAV (robot i) to successfully achieve rendezvous by using relative trajectories that have high informativeness.

- *Tracking through visual occlusions:* Our system enables the UAV to sense the ground robot's spatial direction despite the presence of visual occlusions.
- *Informativeness as a predictor of AOA accuracy:* Iterations 4 and 9, which have high error in AOA_{max} (Eqn. 7), have corresponding high CRB values indicating that these trajectories have low informativeness (Fig. 24). By contrast, low CRB values correctly predict low AOA_{Error}.

Thus our experimental results support our theoretical developments with regards to addressing the moving ends problem, and characterizing the accuracy of measured AOA_{max} as a function of the *informativeness* of a robot's trajectory which is computable using Eqn. (14). Fig. 24 demonstrates the Cramer-Rao Bound (CRB) for each sub-trajectory of the UAV for each SAR iteration during the experiment. The CRB here is obtained via post-processing for the purposes of analysis. We evaluate the CRB here using the true source direction. Future implementations could consider online CRB computation using a *worst-case* source direction which could then be used to *optimize* robot trajectories for improved AOA_{max} estimation. We do not consider trajectory optimization here and rather leave this as an interesting direction of future work.

This proof-of-concept application study demonstrates the applicability of our developed framework to multi-robot tasks (e.g coverage or exploration) that require robots to maintain continuous mobility in an environment with obstacles and visual occlusions. Moreover, use of 3D robot trajectories during the task improves the information quality obtainable by our system.

10 Discussion

In this discussion section we address some practical considerations that need to be taken into account when integrating this system with robot platforms in its current form as well as avenues of improvement and future work.

Practical considerations

Here we address some practical considerations of our work stemming from factors that arise in implementation. We note that discretization of the virtual antenna array elements resulting from a combined effect of trajectory estimation errors and significant WiFi packet loss during transmission, is possible in some implementations. We leave this analysis as an avenue for investigation in future work and in this paper assume that the loss in packet transmission is not severe. For implementation scenarios, a future version of the work could include control of packet transmission as well as optimization of robot trajectories to diminish the occurrence and potential impact of discretization effects.

Future work

Here, we summarize a few directions of interesting future work that could build upon our developed framework and accompanying analysis. Namely we discuss 1) using
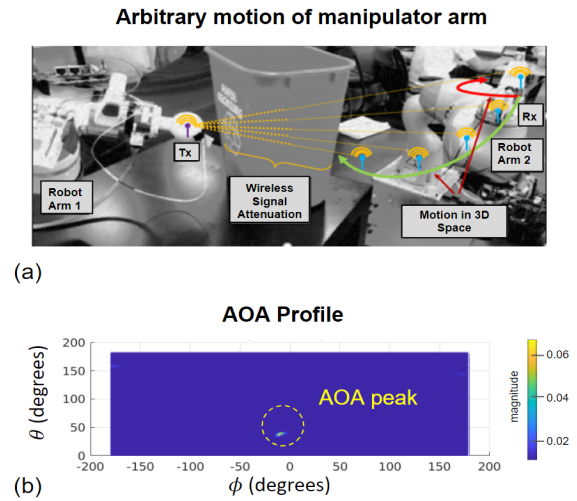
Arbitrary motion of manipulator arm

(a)

AOA Profile

(b)

Figure 25. *Hardware experiment showing a proof-of-concept where an AOA profile is obtained from arbitrary 3D motion of a manipulator arm using the methodologies presented in this paper. Here, a WiFi patch antenna was adhered to the manipulator at the end of the robot arm and ping packets from a second manipulator arm were collected for AOA profile generation. Due to very low estimation error in the trajectory, the resulting AOA profile demonstrates a very clear and almost zero noise peak along the direct path between the two manipulators.*

the measure of informativeness of robot trajectories for *optimization* purposes, 2) the application of our developed framework to collaborative robot perception tasks such as multi-robot mapping and 3) the potential impact of our work on other robotics tasks, including seemingly disparate tasks such as improving manipulation with a robot arm.

Optimizing informativeness: This paper develops the concept of *informativeness* of different robot trajectories for the purpose of obtaining AOA profiles $F_{ij}(\phi, \theta)$ between robots. Interesting avenues of future investigation could include studying the trade-offs between different levels of informativeness and the modification of the robot's natural motion, i.e. co-optimizing the robot trajectories to improve informativeness while achieving their primary coordination task. Additionally using relative trajectories could naturally lead to more informativeness as seen in Sec. 8.2.

Multi-robot perception: The algorithmic framework and analysis presented in this paper addresses sensing over each individual communication link between pairs of robots. One can use this as a basis for *multi-robot* perception where sensed directional profiles can be shared with neighboring robots to achieve several interesting capabilities such as positioning for the entire team, multi-robot mapping without the need for a common reference frame, and/or performing sensor fusion of this information with other more traditional on board sensors such as cameras or LiDARs to learn about the environment.

Robot manipulation: One perhaps surprising outcome of our work on generalizing SAR capabilities to arbitrary 3D robot trajectories, is the applicability of this method to seemingly very different robotic platforms such as robot manipulator arms, that also traverse 3D space along arbitrary trajectories. In fact for these systems, the arbitrary 3D SAR development from this paper can be applied fruitfully, taking advantage of the fact that the manipulator position

in 3D space can be estimated to very high precision using inverse kinematics. Here, a small patch WiFi antenna can be mounted on the tip of the manipulator and used to measure multipath profiles generated by passing WiFi signals through objects in the workspace (such as a closed container), or these profiles can be used to measure the relative direction to another manipulator arm or mobile base for enhanced collaboration abilities. The analysis on informative trajectories developed in this paper can be used to co-optimize manipulator arm motion for enhancing attainable $F_{ij}(\phi, \theta)$, as the manipulator achieves its primary task, such as approaching or manipulating an object. Fig. 25 shows a proof-of-concept where we measured $F_{ij}(\phi, \theta)$ information between two manipulator arms working in unison at the Stanford Robotics Lab in Palo Alto, California.

11 Conclusion

In this paper we develop a system that enables a robot to use local information to obtain spatial information of all other robots on its team with which it can exchange ping packets. Our key idea is to exploit estimated robot trajectories to trace virtual 3D antenna arrays for attaining *continuous* AOA profile generation even in the presence of robot motion at both ends (receiving and transmitting robots). We provide a full theoretical analysis, supported by in-depth experiments, for understanding the informativeness of different robot paths for extracting maximum magnitude path AOA_{max} in the AOA profile from the communication signals, as well as the impact of trajectory estimation error on AOA_{max} accuracy. To our knowledge, this is the most general implementation of such a capability to date. Specifically, our framework is compatible with multi-robot systems that are mobile in 2D and 3D space, are heterogeneous, and must coordinate in potentially cluttered environments with large inter-robot distances as shown by our experimental results and application study.

Declaration of conflicting interests

The Authors declare that there is no conflict of interest.

Notes

1. Code samples used for T265 tracking camera to get position estimates can be found in their github repository : https://github.com/IntelRealSense/librealsense

References

Adib F, Hsu CY, Mao H et al. (2015) Capturing the Human Figure through a Wall. *ACM Trans. Graph.* 34(6). DOI:10.1145/2816795.2818072.

Adib F, Kabelac Z, Katabi D et al. (2014) 3d tracking via body radio reflections. In: *11th USENIX Symposium on Networked Systems Design and Implementation (NSDI 14)*. USENIX Association. ISBN 978-1-931971-09-6, pp. 317–329.

Adib F and Katabi D (2013) See through Walls with WiFi! *Proceedings of the ACM SIGCOMM 2013 Conference on SIGCOMM* : 75–86DOI:10.1145/2486001.2486039.

Almadhoun R, Taha T, Seneviratne L et al. (2019) A survey on multi-robot coverage path planning for model reconstruction and mapping. *SN Applied Sciences* 1(8): 847.

Barrie GB (2004) Through-wall synthetic aperture radar (twsar) 3d imaging: algorithm design. Technical report, DEFENCE RESEARCH AND DEVELOPMENT CANADAOTTAWA (ONTARIO).

Björnson E, Sanguinetti L, Wymeersch H et al. (2019) Massive mimo is a reality—what is next?: Five promising research directions for antenna arrays. *Digital Signal Processing* 94: 3 – 20. DOI:https://doi.org/10.1016/j.dsp.2019.06.007. URL http://www.sciencedirect.com/science/article/pii/S1051200419300776. Special Issue on Source Localization in Massive MIMO.

Burgard W, Moors M, Fox D et al. (2000) Collaborative multi-robot exploration. In: *Proceedings 2000 ICRA. Millennium Conference. IEEE International Conference on Robotics and Automation. Symposia Proceedings (Cat. No.00CH37065)*, volume 1. pp. 476–481 vol.1.

Calvo-Fullana M, Dagefu F, Sadler BM et al. (2019) Multi-mode autonomous communication systems. *2019 53rd Asilomar Conference on Signals, Systems, and Computers* : 1005–1009.

Camposeco F and Pollefeys M (2015) Using vanishing points to improve visual-inertial odometry. In: *2015 IEEE International Conference on Robotics and Automation (ICRA)*. pp. 5219–5225.

Carlone L, Tron R, Daniilidis K et al. (2015) Initialization techniques for 3d slam: A survey on rotation estimation and its use in pose graph optimization. In: *2015 IEEE International Conference on Robotics and Automation (ICRA)*. pp. 4597–4604.

Choudhary S, Carlone L, Nieto C et al. (2017a) Multi robot object-based slam. In: Kulić D, Nakamura Y, Khatib O et al. (eds.) *2016 International Symposium on Experimental Robotics*. Cham: Springer International Publishing. ISBN 978-3-319-50115-4, pp. 729–741.

Choudhary S, Carlone L, Nieto-Granda C et al. (2017b) Distributed mapping with privacy and communication constraints: Lightweight algorithms and object-based models. *The International Journal of Robotics Research* 36: 1286 – 1311.

Cominelli M, Patras P and Gringoli F (2019) Dead on arrival. *Proceedings of the 13th International Workshop on Wireless Network Testbeds, Experimental Evaluation and Characterization - WiNTECH '19* DOI:10.1145/3349623.3355475. URL http://dx.doi.org/10.1145/3349623.3355475.

Cortes J, Martinez S, Karatas T et al. (2004) Coverage control for mobile sensing networks. *IEEE Transactions on Robotics and Automation* 20(2): 243–255.

Cunningham A, Wurm KM, Burgard W et al. (2012) Fully distributed scalable smoothing and mapping with robust multi-robot data association. In: *2012 IEEE International Conference on Robotics and Automation*. IEEE, pp. 1093–1100.

Dhekne A, Gowda M, Zhao Y et al. (2018) Liquid: A wireless liquid identifier. *Proceedings of the 16th Annual International Conference on Mobile Systems, Applications, and Services* .

Fenwick JW, Newman PM and Leonard JJ (2002) Cooperative concurrent mapping and localization. In: *Proceedings 2002 IEEE International Conference on Robotics and Automation (Cat. No.02CH37292)*, volume 2. pp. 1810–1817 vol.2.

Fitch PJ (1988) *Synthetic Aperture Radar*. Springer.

Fox D, Ko J, Konolige K et al. (2006) Distributed multirobot exploration and mapping. *Proceedings of the IEEE* 94(7): 1325–1339. DOI:10.1109/JPROC.2006.876927.

Freda L, Gianni M, Pirri F et al. (2019) 3d multi-robot patrolling with a two-level coordination strategy. *Autonomous Robots* : 1–33.

Gallego G, Rebecq H and Scaramuzza D (2018) A unifying contrast maximization framework for event cameras, with applications to motion, depth, and optical flow estimation. In: *Proceedings of the IEEE Conference on Computer Vision and Pattern Recognition (CVPR)*.

Gautam A, Jha B, Kumar G et al. (2017) Fast - synchronous frontier allocation for scalable online multi-robot terrain coverage. *Journal of Intelligent and Robotic Systems* 87: 545–564.

Gazzah H and Marcos S (2006) Cramer-rao bounds for antenna array design. *IEEE Transactions on Signal Processing* 54: 336–345.

Gil S, Baykal C and Rus D (2019) Resilient multi-agent consensus using wi-fi signals. *IEEE Control Systems Letters* 3: 126–131.

Gil S, Kumar S, Katabi D et al. (2015a) Adaptive communication in multi-robot systems using directionality of signal strength. *The International Journal of Robotics Research* 34: 946 – 968.

Gil S, Kumar S, Mazumder M et al. (2015b) Guaranteeing spoof-resilient multi-robot networks. In: *Proceedings of Robotics: Science and Systems*. Rome, Italy. DOI:10.15607/RSS.2015. XI.020.

Goldsmith A (2005) *Wireless Communications*. USA: Cambridge University Press. ISBN 0521837162.

Gonzalez-Ruiz A and Mostofi Y (2013) Cooperative Robotic Structure Mapping Using Wireless Measurements - A Comparison of Random and Coordinated Sampling Patterns. *IEEE Sensors Journal* 13(7): 2571–2580.

Grisetti G, Kümmerle R, Stachniss C et al. (2010) A tutorial on graph-based slam. *IEEE Transactions on Intelligent Transportation Systems Magazine* 2: 31–43. DOI:10.1109/ MITS.2010.939925.

Guan J, Madani S, Jog S et al. (2020) Through fog high-resolution imaging using millimeter wave radar. *2020 IEEE/CVF Conference on Computer Vision and Pattern Recognition (CVPR)* : 11461–11470.

Ha U, Leng J, Khaddaj A et al. (2020) Food and liquid sensing in practical environments using rfids. In: *17th USENIX Symposium on Networked Systems Design and Implementation (NSDI 20)*. Santa Clara, CA: USENIX Association. ISBN 978-1-939133-13-7, pp. 1083–1100. URL `https://www.usenix.org/conference/nsdi20/presentation/ha`.

Halperin D, Hu W, Sheth A et al. (2010) Predictable 802.11 packet delivery from wireless channel measurements. In: *Proceedings of the ACM SIGCOMM 2010 Conference*, SIGCOMM '10. New York, NY, USA: Association for Computing Machinery. ISBN 9781450302012, p. 159–170. DOI:10.1145/ 1851182.1851203. URL `https://doi.org/10.1145/1851182.1851203`.

Halperin D, Hu W, Sheth A et al. (2011) Tool release: Gathering 802.11n traces with channel state information. *ACM SIGCOMM CCR* 41(1): 53.

Ioannides P and Balanis C (2005) Uniform circular arrays for smart antennas. *IEEE Antennas and Propagation Magazine* 47: 192–206.

Jin H, Wang J, Yang Z et al. (2018) Wish: Towards a wireless shape-aware world using passive rfids. In: *Proceedings of the 16th Annual International Conference on Mobile Systems, Applications, and Services*, MobiSys '18. New York, NY, USA: Association for Computing Machinery. ISBN 9781450357203, p. 428–441. DOI:10.1145/3210240.3210328. URL `https://doi.org/10.1145/3210240.3210328`.

Karanam CR, Korany B and Mostofi Y (2018) Magnitude-Based Angle-of-Arrival Estimation, Localization, and Target Tracking. In: *Proceedings of ACM/IEEE International Conference on Information Processing in Sensor Networks*. pp. 254–265.

Karanam CR and Mostofi Y (2017) 3d through-wall imaging with unmanned aerial vehicles using wifi. *2017 16th ACM/IEEE International Conference on Information Processing in Sensor Networks (IPSN)* : 131–142.

Kotaru M, Joshi K, Bharadia D et al. (2015) Spotfi: Decimeter level localization using wifi. *SIGCOMM Comput. Commun. Rev.* 45(4): 269–282. DOI:10.1145/2829988.2787487. URL `https://doi.org/10.1145/2829988.2787487`.

Krim H and Viberg M (1996) Two decades of array signal processing research: the parametric approach. *IEEE Signal Processing Magazine* 13: 67–94.

Kshirsagar J, Shue S and Conrad JM (2018) A survey of implementation of multi-robot simultaneous localization and mapping. *SoutheastCon 2018* : 1–7.

Kumar S, Gil S, Katabi D et al. (2014a) Accurate indoor localization with zero start-up cost. In: *Proceedings of the 20th annual international conference on Mobile computing and networking*. pp. 483–494.

Kumar S, Hamed E, Katabi D et al. (2014b) Lte radio analytics made easy and accessible. In: *Proceedings of the SIGCOMM '14*.

Ma F and Karaman S (2018) Sparse-to-dense: Depth prediction from sparse depth samples and a single image. In: *2018 IEEE International Conference on Robotics and Automation (ICRA)*. pp. 4796–4803.

Ma Y, Zhou G and Wang S (2019) Wifi sensing with channel state information. *ACM Computing Surveys (CSUR)* 52: 1 – 36.

Manikas A (2004) *Differential Geometry in Array Processing*. Differential Geometry in Array Processing. Imperial College Press. ISBN 9781860944239. URL `https://books.google.com/books?id=6Z0UPauwFCYC`.

Mathews C and Zoltowski M (2020) Signal subspace techniques for source localization with circular sensor arrays. *ECE Technical Reports* .

Mirkin AN and Sibul LH (1991) Cramer-rao bounds on angle estimation with a two-dimensional array. *IEEE Trans. Signal Processing* 39: 515–517.

Mohamed SAS, Haghbayan M, Westerlund T et al. (2019) A survey on odometry for autonomous navigation systems. *IEEE Access* 7: 97466–97486.

Moriya H, Ichige K, Arai H et al. (2012) Novel 3-d array configuration based on crlb formulation for high-resolution doa estimation. In: *2012 International Symposium on Antennas and Propagation (ISAP)*. pp. 1140–1143.

Nigam N, Bieniawski S, Kroo I et al. (2012) Control of multiple uavs for persistent surveillance: Algorithm and flight test results. *IEEE Transactions on Control Systems Technology* 20(5): 1236–1251.

Nobre F, Kasper M and Heckman C (2017) Drift-correcting self-calibration for visual-inertial slam. In: *2017 IEEE International Conference on Robotics and Automation (ICRA)*. pp. 6525–6532. DOI:10.1109/ICRA.2017.7989771.

Orfanidis S (2016) *Electromagnetic Waves and Antennas*. Sophocles J. Orfanidis. URL https://books.google.com/books?id=4n5ezQEACAAJ.

Qin T, Li P and Shen S (2018) Vins-mono: A robust and versatile monocular visual-inertial state estimator. *IEEE Transactions on Robotics* 34: 1004–1020.

S Depatla CRK and Mostofi Y (2017) Robotic Through-Wall Imaging. *IEEE Antenna and Propagation Magazine, special issue on Electromagnetic Inverse Problems for Sensing and Imaging* .

Sabzevari R and Scaramuzza D (2016) Multi-body motion estimation from monocular vehicle-mounted cameras. *IEEE Transactions on Robotics* 32(3): 638–651.

SajadSaeedi G, Trentini M, Seto ML et al. (2016) Multiple-robot simultaneous localization and mapping: A review. *J. Field Robotics* 33: 3–46.

Schmuck P and Chli M (2017) Multi-uav collaborative monocular slam. In: *2017 IEEE International Conference on Robotics and Automation (ICRA)*. pp. 3863–3870.

Schmuck P and Chli M (2019) Ccm-slam: Robust and efficient centralized collaborative monocular simultaneous localization and mapping for robotic teams. *J. Field Robotics* 36: 763–781.

Se S, Lowe D and Little J (2001) Vision-based mobile robot localization and mapping using scale-invariant features. In: *Proceedings 2001 ICRA. IEEE International Conference on Robotics and Automation (Cat. No.01CH37164)*, volume 2. pp. 2051–2058 vol.2.

Solanas A and García MÁ (2004) Coordinated multi-robot exploration through unsupervised clustering of unknown space. *2004 IEEE/RSJ International Conference on Intelligent Robots and Systems (IROS) (IEEE Cat. No.04CH37566)* 1: 717–721 vol.1.

Stump E and Michael N (2011) Multi-robot persistent surveillance planning as a vehicle routing problem. In: *2011 IEEE International Conference on Automation Science and Engineering*. pp. 569–575.

Sturm J, Engelhard N, Endres F et al. (2012) A benchmark for the evaluation of rgb-d slam systems. *2012 IEEE/RSJ International Conference on Intelligent Robots and Systems* : 573–580.

Suleiman A, Zhang Z, Carlone L et al. (2018) Navion: A fully integrated energy-efficient visual-inertial odometry accelerator for autonomous navigation of nano drones. In: *2018 IEEE Symposium on VLSI Circuits*. pp. 133–134.

Suleiman A, Zhang Z, Carlone L et al. (2019) Navion: A 2-mw fully integrated real-time visual-inertial odometry accelerator for autonomous navigation of nano drones. *IEEE Journal of Solid-State Circuits* 54(4): 1106–1119.

Tapus A and Siegwart R (2005) Incremental robot mapping with fingerprints of places. In: *2005 IEEE/RSJ International Conference on Intelligent Robots and Systems*. pp. 2429–2434.

Tse D and Viswanath P (2005) *Fundamentals of Wireless Communication*. USA: Cambridge University Press. ISBN 0521845270.

Twigg J, Dagefu F, Chopra N et al. (2019) Robotic parasitic array optimization in outdoor environments. *2019 IEEE International Symposium on Safety, Security, and Rescue Robotics (SSRR)* : 1–8.

Vasisht D, Kumar S and Katabi D (2016) Decimeter-level localization with a single wifi access point. In: *Proceedings of the 13th Usenix Conference on Networked Systems Design and Implementation*, NSDI'16. USA: USENIX Association. ISBN 9781931971294, p. 165–178.

Verma G, Dagefu F, Sadler BM et al. (2018) Doa estimation for autonomous systems in complex propagation environments. *2018 IEEE 19th International Workshop on Signal Processing Advances in Wireless Communications (SPAWC)* : 1–5.

Vu D, Renaux A, Boyer R et al. (2011) A cramér rao bounds based analysis of 3d antenna array geometries made from ula branches. *Multidimensional Systems and Signal Processing* 24: 1–35. DOI:10.1007/s11045-011-0160-5.

Vu DT, Renaux A, Boyer R et al. (2010) Performance analysis of 2d and 3d antenna arrays for source localization. *2010 18th European Signal Processing Conference* : 661–665.

Wang J and Katabi D (2013) Dude, where's my card? rfid positioning that works with multipath and non-line of sight. In: *Proceedings of the ACM SIGCOMM 2013 Conference on SIGCOMM*, SIGCOMM '13. New York, NY, USA: Association for Computing Machinery. ISBN 9781450320566, p. 51–62. DOI:10.1145/2486001.2486029. URL https://doi.org/10.1145/2486001.2486029.

Wang W, Jadhav N, Vohs P et al. (2019) Active rendezvous for multi-robot pose graph optimization using sensing over wi-fi. *International Symposium on Robotics Research* .

Watts C, Lancaster P, Pedross-Engel A et al. (2016) 2d and 3d millimeter-wave synthetic aperture radar imaging on a pr2 platform. *2016 IEEE/RSJ International Conference on Intelligent Robots and Systems (IROS)* : 4304–4310.

Wheeler T, Bharathi E and Gil S (2019) Switching topology for resilient consensus using wi-fi signals. In: *2019 International Conference on Robotics and Automation (ICRA)*. pp. 2018–2024.

Xiong J and Jamieson K (2013a) Arraytrack: A fine-grained indoor location system. In: *Proceedings of the 10th USENIX Conference on Networked Systems Design and Implementation*, nsdi'13. USA: USENIX Association, p. 71–84.

Xiong J and Jamieson K (2013b) Securearray: Improving wifi security with fine-grained physical-layer information. In: *Proceedings of the 19th Annual International Conference on Mobile Computing and Networking*, MobiCom '13. New York, NY, USA: Association for Computing Machinery. ISBN 9781450319997, p. 441–452. DOI:10.1145/

2500423.2500444. URL https://doi.org/10.1145/2500423.2500444.

Yang Z, Zhou Z and Liu Y (2013) From rssi to csi: Indoor localization via channel response. *ACM Comput. Surv.* 46: 25:1–25:32.

Zhang D, Wang J, Jang J et al. (2019) On the feasibility of wi-fi based material sensing. In: *The 25th Annual International Conference on Mobile Computing and Networking*, MobiCom '19. New York, NY, USA: Association for Computing Machinery. ISBN 9781450361699. DOI:10.1145/3300061.3345442. URL https://doi.org/10.1145/3300061.3345442.

Zhu X and Feng Y (2013) Rssi-based algorithm for indoor localization. *Communications and Network* 05: 37–42.

APPENDIX

A   Cramer Rao Bound Development

I. Spherical Helix Trajectory: We parameterize a spherical helix in spherical coordinates as given by:

$$\xi_u = \tau, \quad \varphi_u = c\tau, \quad \rho_u = r$$

for a spherical helix of radius r, spiral climb rate of c, and parameterization $\tau \in [0, 2\pi)$. We assume that each antenna element u is uniformly spaced along the helix so that $\tau = u = \{0, \Delta, 2\Delta, \ldots, (M-1)\Delta\}$ where $\Delta = \frac{2\pi}{M}$. Further, we assume a climb rate $c = 1$ for a simplification of our closed form, though any constant can be similarly substituted before integration. We set M approaching infinity (i.e. assume a very large number of packets received) to simplify analysis. So for our 3D spherical helical trajectory, our CRB terms are:

$$\mathbf{A} = \frac{\partial \mathbf{a}^H(\theta, \phi) \partial \mathbf{a}(\theta, \phi)}{\partial \theta \partial \theta} =$$

$$\sum_{u=1}^{M} \frac{4\pi^2 r^2}{\lambda^2} (\cos\theta \sin((u-1)\Delta) \cos(\phi - c(u-1)\Delta)$$
$$- \cos((u-1)\Delta) sin(\theta))^2$$

Setting $M \to \infty, c = 1$ we get

$$\mathbf{A} = -\frac{\pi^2 r^2 \left(\cos^2(\theta) \cos(2\phi) + \cos(2\theta) - 3 \right)}{\lambda^2}$$

$$\mathbf{B} = \frac{\partial \mathbf{a}^H(\theta, \phi) \partial \mathbf{a}(\theta, \phi)}{\partial \phi \partial \phi} =$$

$$\sum_{u=1}^{M} \frac{4\pi^2 r^2}{\lambda^2} (\sin\theta \sin((u-1)\Delta) \sin(\phi - c(u-1)\Delta)))^2$$

Setting $M \to \infty, c = 1$ we get

$$\mathbf{B} = \frac{\pi^3 r^2 \sin^2(\theta)(\cos(2\phi) + 2)}{\lambda^2}$$

$$\mathbf{C} = \frac{\partial \mathbf{a}^H(\theta, \phi) \partial \mathbf{a}(\theta, \phi)}{\partial \phi \partial \theta} =$$

$$\sum_{u=1}^{M} \frac{4\pi^2 r^2}{\lambda^2} (\cos\theta \sin((u-1)\Delta) \cos(\phi - c(u-1)\Delta))$$
$$- \cos((u-1)\Delta) \sin\theta)(\sin\theta \sin((u-1)\Delta)$$
$$* \sin(\phi - c(u-1)\Delta))$$

Setting $M \to \infty, c = 1$ we get

$$\mathbf{C} = \frac{2\pi^3 r^2 \sin(\theta) \cos(\theta) \sin(\phi) \cos(\phi)}{\lambda^2}.$$

II. Planar Circular Trajectory: We parameterize a planar circle as follows:

$$\xi_u = \tau, \quad \rho_u = r, \quad \varphi_u = \cos^{-1}(0) = \pi/2$$

The CRB equations reduce to

$$\mathbf{A} = \sum_{u=1}^{M} \frac{4\pi^2 r^2}{\lambda^2} \cos^2\theta \cos^2(\phi - (u-1)\Delta)$$

$$= \frac{4\pi^2 r^2}{\lambda^2} \cos^2\theta \sum_{u=1}^{M} (\frac{1}{2} + \frac{\cos(2\phi - 2(u-1)\Delta)}{2})$$

Setting $M \to \infty$, we get

$$\mathbf{A} = \frac{2\pi^2 r^2}{\lambda^2} \cos^2\theta$$

and

$$\mathbf{B} = \sum_{u=1}^{M} \frac{4\pi^2 r^2}{\lambda^2} \sin^2\theta \sin^2(\phi - (u-1)\Delta)$$

$$= \frac{4\pi^2 r^2}{\lambda^2} \sin^2\theta \sum_{u=1}^{M} (\frac{1}{2} - \frac{\cos(2\phi - 2(u-1)\Delta)}{2})$$

Setting $M \to \infty$, we get

$$\mathbf{B} = \frac{2\pi^2 r^2}{\lambda^2} \sin^2\theta$$

and finally,

$$\mathbf{C} = \sum_{u=1}^{M} -\frac{4\pi^2 r^2}{\lambda^2} \cos\theta \cos(\phi - (u-1)\Delta)$$
$$\times (\sin\theta \sin(\phi - (u-1)\Delta))$$

$$= -\frac{4\pi^2 r^2}{\lambda^2} \cos\theta \sin\theta \sum_{u=1}^{M} \sin(2\phi - 2(u-1)\Delta)$$

Setting $M \to \infty$, we get

$$\mathbf{C} = 0.$$

B   Notations and Terminology

Coordinate System

$(\hat{\phi}, \hat{\theta})$ Estimated relative AOA to the transmitting robot (AOA peak in $F_{ij}(\phi, \theta)$)

$(\rho_i(t), \varphi_i(t), \xi_i(t))$ spherical coordinates of receiving robot's position denoting displacement, azimuth and elevation angles wrt. the first position in its trajectory $\chi_i(\mathbf{t})$

(ϕ, θ) signal transmitting robot's relative azimuth and elevation direction wrt. the initial position of the receiving robot

(ϕ_g, θ_g) True AOA (obtained from motion capture system) between transmitting and receiving robot

t time

$p_i(t)$ groundtruth position of the robot i at time t

$(\kappa_\rho, \kappa_\phi, \kappa_\theta)$ position estimation error in ρ, ϕ, θ accordingly in polar coordinates

δ deviation around κ_ϕ in azimuth

μ deviation around κ_θ in elevation

δ_{max} max deviation around κ_ϕ in azimuth

μ_{max} max deviation around κ_θ in elevation

δ_u deviation around κ_ϕ in azimuth at position $p_i(t_u)$

μ_u deviation around κ_θ in elevation at position $p_i(t_u)$

$\hat{p}_i(t_k)$ Estimated position estimate of robot i at time t obtained from T265 tracking camera

Robot Trajectory

$\chi_i(t_k)$ Ground truth pose of robot i at time t_k

$\hat{\chi}_i(t_k)$ Estimated pose of robot (obtained from on-board VIO sensor or by adding simulated gaussian noise) i at time t_k

$\boldsymbol{\chi_i(t)}$ Local groundtruth sub-trajectory of robot i for $t \in [t_k, \ldots, t_l]$ which is a vector of positions $\chi_i(t)$

$\boldsymbol{\hat{\chi}_i(t)}$ Local estimated sub-trajectory of robot i for $t \in [t_k, \ldots, t_l]$ which is a vector of positions $\hat{\chi}_i(t)$

$\mathcal{N}_i$ all transmitting robots for which robot i can hear ping packets from

$R_i(t)$ Orientation of the robot i at time t

$R_\epsilon(t)$ Accumulated error in robot orientation $R_i(t)$ at time t

$p_\epsilon(t_k)$ Accumulated error in robot position $p_i(t)$ at time t

$(x_i(t), y_i(t), z_i(t))$ Robot position $p_i(t)$ in cartesian coordinates

$SO(3)$ Special Orthogonal group in 3D

$\mathbb{R}^3$ Euclidean space in 3D

$\epsilon(t)$ Residual error

$\boldsymbol{\chi_{ij}(t)}$ Relative trajectory of robot i wrt. robot j

$\boldsymbol{\tilde{\chi}_i(t)}$ Rotated trajectory with respect to true NORTH and DOWN direction

$\tilde{R}_i$ Rotation offset of robot i's coordinate frame with respect to true NORTH and true DOWN direction

$\tilde{t}_{ij}$ Translation offset between robot i and robot j

Synthetic Aperture Radar

λ Wireless signal wavelength

$h_{ij}(t)$ Wireless signal measurements between signal transmitting robot j and receiving robot i

$d_{ij}(t)$ Ground truth distance between robot positions $p_i(t)$ and $p_j(t)$

$\mathbf{Y_{ij}(t)}$ Multi-antenna array output observation model

$Y(t_k)$ Received signal at robot position $p_i(t_k)$

$\mathbf{a}(\theta, \phi)\mathbf{(t)}$ Steering Vector

$\mathbf{n(t)}$ Received signal noise vector

M Number of received signal packets

$\mathbf{h_{ij}(t)}$ Wireless channel

$F_{ij}(\phi, \theta)$ AOA profile, refers to relative paths a WiFi signal traverses between a given pair of signal transmitting robot j and receiving robot i It is thus a 2D matrix calculated for all possible incoming signal directions along azimuth and elevation (360 x 180).

σ^2 Variance in signal noise

I Identity matrix

$\|h\|$ Magnitude of wireless signal

$a(\theta, \phi)(t)$ Element of steering vector $\mathbf{a}(\theta, \phi)\mathbf{(t)}$ at time t

AOA_{max} Strongest signal direction i.e maximum magnitude path, in the full AOA profile $F_{ij}(\phi, \theta)$

Δ_f Frequency offset

$h_{ij}^r(t)$ Reverse wireless signal channel between robot i and robot j

$\hat{h}_{ij}(t)$ Observed forward wireless channel

$\hat{h}_{ij}^r(t)$ Observed reverse wireless channel

A, B, C   Partial derivative terms in Cramer Rao Bound formulation for trajectory informativeness.

FIM   Fisher Information Matrix

SNR   Signal To Noise Ration

Δ $\frac{2\pi}{M}$

τ Uniform spacing between antenna elements used for CRB analysis of special geometries.

c   climb rate for simulated trajectories

Det   Determinant

$\angle F(\phi, \theta)$ Phase component of the AOA profile $F_{ij}(\phi, \theta)$